

SIMULATING WAVES IN THE UPPER SOLAR ATMOSPHERE WITH SURYA: A WELL-BALANCED HIGH-ORDER FINITE VOLUME CODE.

F. G. FUCHS, A. D. MCMURRY, S. MISHRA, AND K. WAAGAN

ABSTRACT. We consider propagation of waves in a stratified non-isothermal magnetic atmosphere. The situation of interest corresponds to waves in the outer solar (chromosphere and corona) and other stellar atmospheres. The waves are simulated by using a high-resolution, well-balanced finite volume based massively parallel code termed SURYA. Numerical experiments in both two and three space dimensions involving realistic temperature distributions, driving forces and magnetic field configurations are described. Diverse phenomena like mode conversion, wave acceleration at the transition layer and driving dependent wave dynamics are observed. We obtain evidence for the presence of coronal Alfvén waves in some three dimensional configurations. Although some of the incident wave energy is transmitted into the corona, a large proportion of it is accumulated in the chromosphere providing a possible mechanism for chromospheric heating.

1. INTRODUCTION

Waves and oscillations are a significant means for the transport and circulation of energy in gravitationally stratified highly conducting astrophysical plasmas. Examples include waves emitted by localized sources within magnetic flux concentrations such as acoustic sources in the Sun's magnetic network and within isolated magnetic flux tubes, knots and sunspots. Other examples pertain to waves in late type stars and planetary magneto-atmospheres. The study of wave propagation improves our understanding of the dynamical processes in the solar and other stellar atmospheres and contributes to explanations for phenomena like coronal and chromospheric heating and internetwork oscillations.

Extensive studies of the waves in the solar atmosphere have been performed with observations from telescopes like the Swedish solar telescope and with satellites like SOHO and HINODE (Banerjee *et al.* 2007). These observational tools have also provided a good deal of information about the detailed magnetic structure of the sun. In particular, Van der Voort *et al.* (2005) show that the granular flow emanating from the solar convection zone arranges the magnetic flux into sheets that are visible as thin bright features. These flux sheets are characterized by weak upflows of the plasma inside them as well as strong downflows in the surrounding medium. The flux sheets are also subject to instabilities. It is well known that convection results in the excitation of acoustic waves at the base of the photosphere. Furthermore, the magnetic instabilities in the photosphere excite magnetic modes resulting in a complex wave pattern at the base of the photosphere.

Once generated at the photospheric level, the waves travel up the chromosphere and into the corona while interacting with the magnetic field in a complicated manner. Observational results have been obtained in McIntosh *et al.* (2002, 2003, 2004), Finsterle *et al.* (2004) and references therein. In McIntosh *et al.* (2002, 2003) the authors have found a strong correlation between observations of wave power from SOHO (SUMER) and the magnetic field topology from SOHO (MDI). The behavior of the observed wave modes in the chromosphere and the corona has been used as a tool to predict the magnetic field topology. Such predictions were presented in Finsterle *et al.* (2004) for the chromosphere and in McIntosh *et al.* (2004) for the the corona.

Date: January 19, 2011.

Key words and phrases. Stratified MHD, Non-isothermal atmospheres, Well balanced schemes.

Acknowledgements: The authors thank the anonymous referee for suggestions which greatly improved the contents and presentation of this paper. K. Waagan is partially supported by NSF grants DMS07-07949, DMS10-08397 and ONR grant N000140910385.

Another interesting phenomenon that the observations have revealed is the existence of periodic and spatially coherent motions in the photosphere and lower chromosphere. These motions have a peak in power at around 5 minutes in the photosphere. Different 5 minute periodic motions in the chromosphere, transition region and corona have been reported in a series of papers, see De Pontieu *et al.* (2003a,b), Finsterle *et al.* (2008) and references therein.

Despite the wealth of observational data, it is not yet possible to build a consistent dynamic view of the chromosphere due to the complex wave behavior and wave-magnetic field interaction. We need to model the conditions in the chromosphere and corona and use extensive numerical simulations to better understand the observations.

Theoretical studies of wave propagation in stratified magneto-atmospheres have been performed over the last two decades. The most popular modeling framework is based on the equations of magnetohydrodynamics (MHD) in a stratified medium. These equations are a non-linear system of PDEs and analytical solutions are not possible, except in the simplest of cases. In Zhugzhda & Dzhalilov (1984a,b), the authors obtained analytical solutions for waves propagating in an isothermal atmosphere with an oblique magnetic field. More recent analytical studies were performed by Cally (2001, 2006) by using ray tracing. These analytical studies are limited by the simplifying assumptions which do not hold in a realistic magneto-atmosphere. Hence, numerical simulations are the key tools to study wave propagation in the solar atmosphere.

The design of robust numerical methods for stratified MHD equations is quite challenging. The non-linearity implies that solutions may contain discontinuities in the form of shock waves. The shock structure of MHD is quite complicated as the equations are neither strictly hyperbolic nor convex (Toth 2000). Furthermore, MHD codes have to handle the divergence constraint in a suitable manner in order to avoid numerical instabilities. Waves are modeled as *small* perturbations of steady states of the stratified MHD equations. The numerical method must be able to capture these perturbations. Well balanced schemes i.e, schemes which preserve a discrete version of the steady state are well suited for such simulations (Fuchs *et al.* 2010b). Furthermore, suitable non-reflecting numerical boundary conditions need to be implemented as the top boundary computational domain has to be truncated artificially at the top. An elaborate description of these difficulties is provided in Fuchs *et al.* (2010b, 2011b).

Numerical simulations of waves in the solar atmosphere have been presented in a number of papers in recent years. A very partial list includes Rosenthal *et al.* (2002), Bogdan *et al.* (2003), Hasan & Ballegoijen (2007, 2008), Hansteen *et al.* (2006, 2007), Erdelyi *et al.* (2007), Khomenko *et al.* (2008), Fedun *et al.* (2009), Carlsson & Bogdan (2006) and references therein. In Rosenthal *et al.* (2002) and Bogdan *et al.* (2003), the authors study a two-dimensional isothermal atmosphere numerically using a modified STAGGER finite difference code of Nordlund & Galsgaard (1995). They obtain numerical evidence for the conversion of slow mode waves into a combination of slow and fast waves at the magnetic canopy i.e at plasma $\beta = 1.2$. In Bogdan *et al.* (2003), the authors consider a three dimensional stratified isothermal atmosphere and simulate planar waves, using a magnetic field extrapolated from SOHO/MDI observations. The authors demonstrate the crucial role played by the angle between the magnetic field and the incident wave front at the canopy. More recent developments in this direction are contained in Hansteen *et al.* (2006).

In Fedun *et al.* (2009), the authors simulate a three dimensional magneto-atmosphere using a modified version of the VAC code of Toth (2000). The configuration includes both the chromosphere and the corona with a temperature profile similar to the VAL IIIIC model (Vernazza *et al.* 1981). The background magnetic field is taken to be a very simple constant upward pointing magnetic field. One of the key issues studied in Fedun *et al.* (2009) is the role that driving frequency plays in the wave propagation.

Given that most of the numerical studies have focused on either simulating the chromosphere with a realistic magnetic field or on simulating the chromosphere, transition region and corona but with a simplistic magnetic field, we present numerical simulations for a three dimensional realistic solar atmosphere from the photosphere to the corona. The aim of this paper is to describe a code for simulating the solar atmosphere. This code termed *SURYA* has the following properties:

- (i.) It is a robust high order finite volume scheme based on approximate Riemann solvers of the HLL type.
- (ii.) The code can handle both two and three dimensional configurations.
- (iii.) The divergence constraint is implemented through an upwind discretization of the Godunov-Powell source term for ideal MHD equations (Fuchs *et al.* 2011a).
- (iv.) The finite volume schemes are well-balanced i.e they preserve discrete equilibrium states for non-isothermal atmospheres.
- (v.) Realistic temperature profiles, background magnetic fields and photospheric driving are incorporated.
- (vi.) Neumann type numerical boundary conditions (Fuchs *et al.* 2010a) are employed at the top boundary.
- (vii.) The code is implemented on massively parallel architectures.

Many features of the code are novel. In particular, the code is based on the first well-balanced schemes for stratified MHD equations (Fuchs *et al.* 2010b, 2011b).

We perform and report several numerical simulations with *SURYA* in this paper. The simulations are based on

- A non-isothermal stratified MHD model that includes a synthetic (inspired by the VAL-IIC) temperature profile for the chromosphere and the corona.
- Synthetic magnetic fields (following Bogdan *et al.* 2003) in both two and three space dimensions.
- A magnetic field extrapolated from SOHO/MDI that can replace the three-dimensional synthetic field.
- Photospheric driving mechanisms of different types and with different frequencies.

We focus on how the waves induced at the photosphere travel up the chromosphere and the corona and how they interact with the underlying magnetic field. In particular, we focus on how much energy these waves carry up the atmosphere and deposit in the chromospheric and coronal plasmas. A related issue that we address is the role played by the frequency of the driving in the energy transfer. Most of the analysis is performed in two space dimensions and with synthetic magnetic fields in three dimensions. We also include a simulation with an extrapolated magnetic field from SOHO/MDI observations and with photospheric driving, also from SOHO data, in order to demonstrate the ability of our code to handle realistic scenarios.

The rest of this paper is organized as follows: in section 2, we present the model equations and the steady states of interest. The numerical schemes are described in section 3 and in Appendix A. Numerical simulations in two and three dimensions are presented in sections 4 and 5, respectively.

2. THE MODEL

We model the outer solar atmosphere with a modified version of the stratified MHD equations (Fuchs *et al.* 2010b). In non-dimensionalized form, the governing equations are

$$\begin{aligned}
 (2.1) \quad & \rho_t + \operatorname{div}(\rho \mathbf{u}) = 0, \\
 & (\rho \mathbf{u})_t + \operatorname{div} \left(\rho \mathbf{u} \otimes \mathbf{u} + \left(p + \frac{1}{2} |\mathbf{B}|^2 + \tilde{\mathbf{B}} \cdot \mathbf{B} \right) \mathbf{I} - \mathbf{B} \otimes \mathbf{B} - \tilde{\mathbf{B}} \otimes \mathbf{B} - \mathbf{B} \otimes \tilde{\mathbf{B}} \right) \\
 & \qquad \qquad \qquad = - \left(\mathbf{B} + \tilde{\mathbf{B}} \right) (\operatorname{div} \mathbf{B}) - \rho g \mathbf{e}_3, \\
 & \mathbf{B}_t + \operatorname{div} \left(\mathbf{u} \otimes \mathbf{B} - \mathbf{B} \otimes \mathbf{u} + \mathbf{u} \otimes \tilde{\mathbf{B}} - \tilde{\mathbf{B}} \otimes \mathbf{u} \right) = -\mathbf{u}(\operatorname{div} \mathbf{B}), \\
 & E_t + \operatorname{div} \left(\left(E + p + \frac{1}{2} |\mathbf{B}|^2 + \mathbf{B} \cdot \tilde{\mathbf{B}} \right) \mathbf{u} - (\mathbf{u} \cdot \mathbf{B}) \mathbf{B} - (\mathbf{u} \cdot \tilde{\mathbf{B}}) \mathbf{B} \right) \\
 & \qquad \qquad \qquad = -(\mathbf{u} \cdot \mathbf{B})(\operatorname{div} \mathbf{B}) - \rho g (\mathbf{u} \cdot \mathbf{e}_3).
 \end{aligned}$$

Here, ρ is the density, $\mathbf{u} = (u_1, u_2, u_3)$ the velocity, p the thermal pressure, g the constant acceleration due to gravity, and \mathbf{e}_3 represents the unit vector in the vertical (z -) direction. The total magnetic field is $\mathbf{B} + \tilde{\mathbf{B}}$, where $\mathbf{B} = (B_1, B_2, B_3)$ is the deviation from a background potential field

$\tilde{\mathbf{B}}$, i.e. $\tilde{\mathbf{B}}$ satisfies the following assumptions,

$$(2.2) \quad \tilde{\mathbf{B}}_t = 0, \quad \operatorname{div}(\tilde{\mathbf{B}}) = 0, \quad \text{and} \quad \operatorname{curl}(\tilde{\mathbf{B}}) = 0.$$

The total energy E is determined by the ideal gas equation of state:

$$E = \frac{p}{\gamma - 1} + \frac{1}{2} |\mathbf{B}|^2 + \frac{1}{2} \rho |\mathbf{u}|^2.$$

Writing (2.1) as a balance law explicitly, we obtain,

$$(2.3) \quad \mathbf{U}_t + (\mathbf{f}(\mathbf{U}, \tilde{\mathbf{B}}))_x + \mathbf{g}(\mathbf{U}, \tilde{\mathbf{B}})_y + \mathbf{h}(\mathbf{U}, \tilde{\mathbf{B}})_z = \mathbf{s}^1(\mathbf{U}, \tilde{\mathbf{B}}) + \mathbf{s}^2(\mathbf{U}, \tilde{\mathbf{B}}) + \mathbf{s}^3(\mathbf{U}, \tilde{\mathbf{B}}) + \mathbf{s}^g(\mathbf{U}),$$

where

$$\mathbf{U} = \{\rho, \rho u_1, \rho u_2, \rho u_3, B_1, B_2, B_3, E\}$$

is the vector of conserved variables and $\tilde{\mathbf{B}} = \{\tilde{B}_1, \tilde{B}_2, \tilde{B}_3\}$ is the background magnetic field. The fluxes $\mathbf{f}, \mathbf{g}, \mathbf{h}$, Godunov-Powell source terms $\mathbf{s}^{1,2,3}$ and the gravity source term \mathbf{s}^g can be read from (2.1).

2.1. Steady states. We construct equilibrium solutions of (2.1) by setting the velocity \mathbf{u} and the magnetic field deviation \mathbf{B} to zero. From the ideal gas equation of state, we obtain

$$(2.4) \quad p = gH\rho T,$$

for a constant H and the temperature T . We assume that the steady state temperature $T = T(z)$ varies only in the vertical direction. Substituting (2.4) in (2.1) and assuming $\mathbf{u} = 0$ leads to

$$(2.5) \quad \frac{dp}{dz} = -\frac{p}{HT(z)}.$$

Solving the above equation explicitly yields

$$p(x, y, z) = p(z) = p_0 e^{-\frac{\alpha(z)}{H}}.$$

Here, p_0 is a constant and

$$(2.6) \quad \alpha(x, y, z) = \alpha(z) = \int_0^z \frac{1}{T(s)} ds.$$

Similarly, we can calculate the steady state density as

$$\rho(x, y, z) = \rho(z) = \frac{\rho_0 T_0}{T(z)} e^{-\frac{\alpha(z)}{H}},$$

with (ρ_0, T_0) being constant. Combining the above expressions, we obtain the steady state:

$$(2.7) \quad \mathbf{u} \equiv \mathbf{0}, \quad \mathbf{B} \equiv \mathbf{0} \quad \rho(z) = \frac{\rho_0 T_0}{T(z)} e^{-\frac{\alpha(z)}{H}}, \quad p(z) = p_0 e^{-\frac{\alpha(z)}{H}}.$$

The steady state pressure and density are scaled in terms of the function α which in turn depends on the temperature. Furthermore α is a monotonically increasing function as the temperature is always positive. In the simplest case of an isothermal atmosphere, i.e., $T \equiv \tilde{T}$ for some constant \tilde{T} , the expression (2.7) simplifies as

$$(2.8) \quad \mathbf{u} \equiv \mathbf{0}, \quad \mathbf{B} \equiv \mathbf{0}, \quad \rho(x, y, z) = \rho_0 e^{-\frac{z}{\tilde{T}H}}, \quad p(x, y, z) = p_0 e^{-\frac{z}{\tilde{T}H}},$$

and the pressure and density decay exponentially.

2.1.1. Hydrodynamic steady state. We obtain a purely hydrodynamic steady state by assuming that the background magnetic field is

$$(2.9) \quad \tilde{\mathbf{B}} \equiv \mathbf{0}.$$

2.1.2. *Magnetic steady states.* Non-trivial solutions of (2.2) lead to interesting magnetic steady states. Note that solutions of (2.2) can be characterized by vector harmonic functions.

In three space dimensions, a Fourier solution of (2.2) can be written down explicitly as, (2.10)

$$\begin{aligned}\tilde{B}_1(x, y, z) &= \sum_{l=1}^L \sum_{m=0}^M \frac{l \alpha_{lm}}{\sqrt{l^2 + m^2}} e^{-2\pi\sqrt{l^2+m^2}z} \left(a_{lm} \sin(2\pi lx) \cos(2\pi my) - b_{lm} \cos(2\pi lx) \sin(2\pi my) \right. \\ &\quad \left. - c_{lm} \cos(2\pi lx) \cos(2\pi my) + d_{lm} \sin(2\pi lx) \sin(2\pi my) \right), \\ \tilde{B}_2(x, y, z) &= \sum_{l=0}^L \sum_{m=1}^M \frac{m \alpha_{lm}}{\sqrt{l^2 + m^2}} e^{-2\pi\sqrt{l^2+m^2}z} \left(a_{lm} \cos(2\pi lx) \sin(2\pi my) - b_{lm} \sin(2\pi lx) \cos(2\pi my) \right. \\ &\quad \left. + c_{lm} \sin(2\pi lx) \sin(2\pi my) - d_{lm} \cos(2\pi lx) \cos(2\pi my) \right), \\ \tilde{B}_3(x, y, z) &= \sum_{l=0}^L \sum_{m=0}^M \alpha_{lm} e^{-2\pi\sqrt{l^2+m^2}z} \left(a_{lm} \cos(2\pi lx) \cos(2\pi my) + b_{lm} \sin(2\pi lx) \sin(2\pi my) \right. \\ &\quad \left. + c_{lm} \sin(2\pi lx) \cos(2\pi my) + d_{lm} \cos(2\pi lx) \sin(2\pi my) \right).\end{aligned}$$

Here, $a_{lm}, b_{lm}, c_{lm}, d_{lm}$ are the Fourier coefficients corresponding to the background magnetic field $\tilde{B}_3(x, y, 0)$ at the bottom of the domain, and L, M are the maximum number of modes for the indices l and m respectively. The factor α_{lm} is $1/4$ if $l = m = 0$, $1/2$ if l or m is zero, and 1 otherwise. It can be readily checked that (2.10) satisfies (2.2). See also Fuchs *et al.* (2010a,b) for a two dimensional version.

3. THE CODE

We approximate (2.1) with a second-order accurate finite volume scheme. The scheme has the added advantage of being well balanced i.e, it preserves a discrete version of the steady state (2.7) for any background magnetic field $\tilde{\mathbf{B}}$ satisfying (2.2) and for any steady state temperature distribution $T = T(z)$. The scheme is described in detail in Appendix A.

This well-balanced high-order scheme is implemented in a modular C++ based code termed *SURYA*¹. The code includes a set of approximate Riemann solvers, high-order non-oscillatory reconstruction and time integration routines. Realistic initial and boundary conditions are also specified. A wide range of background magnetic fields $\tilde{\mathbf{B}}$ are included. The code is parallelized with the MPI library, using a domain decomposition technique. The parallelization is straightforward as the schemes are explicit and do not need any staggered grids. A python front end to the code is included for configuring data and results are visualized using matplotlib for two-dimensional simulations and MAYAVI2 for three-dimensional simulations. All the results presented below are from experiments performed on the TITAN cluster of the University of Oslo and on the STALLO cluster of the University of Tromsø.

4. NUMERICAL RESULTS IN TWO SPACE DIMENSIONS

All the quantities that appear in (2.1) are non-dimensionalized suitably from the realistic solar parameters used in Bogdan *et al.* (2003), shown in table 1. The constants are acceleration due to gravity, $g = 2.74$, the thermodynamical parameter $H = 0.158$ and bottom initial pressure $p_0 = 1.13$. All subsequent two-dimensional experiments are performed on the domain $[x, z] \in [0, 4] \times [0, 8]$.

4.1. **Temperature profile:** We use a temperature profile for the chromosphere and corona that is based on the VAL-IIIIC model (Vernazza *et al.* 1981), see figure 1 (left panel). We fit the following

¹<http://folk.uio.no/mcmurry/amhd/>

TABLE 1. Units used in this paper

Quantity	CGS units
length	10^8 cm
time	10^2 s
velocity	10^6 cm s $^{-1}$
pressure	10^5 g cm $^{-1}$ s $^{-2}$
density	10^{-11} g cm $^{-3}$
magnetic field	1120 G

(simplified) temperature profile,

$$T(z) = \begin{cases} 1, & \text{if } z \leq 1 \\ +792(z-1)^2 + 1, & \text{if } 1 < z \leq 1.25 \\ -792(z-1.5)^2 + 100, & \text{if } 1.25 < z \leq 1.5 \\ 100, & \text{if } 1.5 < z \end{cases}$$

to the VAL-IIIC profile. The domain starts from the photosphere and continues through the chromosphere into the corona. The transition region is between $z = 1$ and $z = 1.5$. The equations solved in our code will not accurately represent coronal physics. In this paper we are interested in the waves that are transmitted through the transition region, rather than in coronal dynamics.

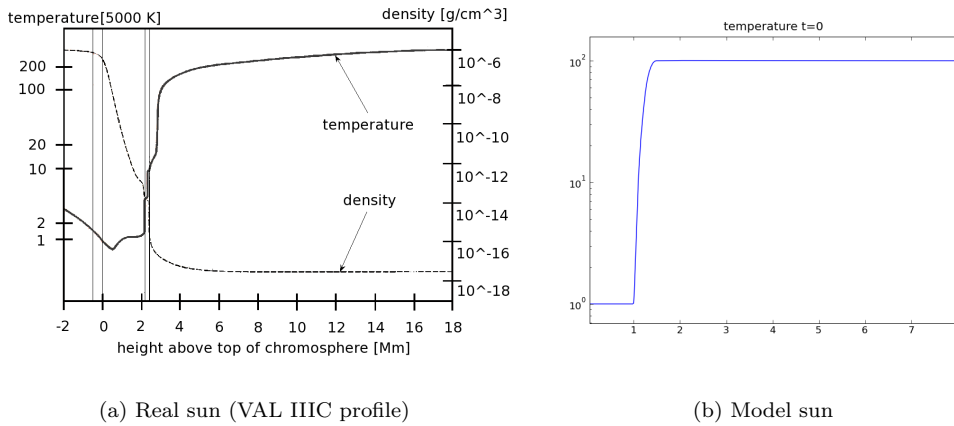


FIGURE 1. Steady state temperature distribution for the real and model solar atmospheres.

4.2. Background magnetic field. In two space dimensions, we choose a *realistic* two-dimensional background magnetic field of the form (2.10) as follows: We let $\tilde{B}_3(x, 0, 0)$ approximate

$$(4.1) \quad \tilde{B}_3(x, 0, 0) = 2.7e^{-7.2r^2} - 1.3e^{-40(r-0.6)^2}, \quad r = |x - 2|, x \in [0, 4]$$

up to the first fourteen terms in the Fourier series. The full magnetic field $\tilde{\mathbf{B}}(x, y, z)$ follows from the potential field assumption as in (2.10). The resulting potential field consists of a large unipolar magnetic flux concentration surrounded on each side by two smaller concentrations of opposite polarity field (Bogdan *et al.* 2003, figure 1 for an illustration). The initial conditions are set to the steady state (2.7). We consider the following configurations:

4.3. High frequency planar waves with vertical forcing. With the above background temperature profile and magnetic field, we excite planar waves at the bottom boundary by prescribing

$$(4.2) \quad \mathbf{u}(x, 0, t) = (0, 0, 0.1 \sin(2\pi\omega t))^T.$$

Here, the frequency of the driving is the parameter ω . For our first experiment, we choose $\omega = 3.0$. In figure 2, we plot time snapshots (at different time levels) of the velocity component parallel to the magnetic field and the velocity component perpendicular to the magnetic field. The plots show the planar waves, excited at the photosphere, traveling up the chromosphere and into the corona. The velocity in the direction of the magnetic field is an indicator of both slow and fast mode waves (Bogdan *et al.* 2003) whereas the velocity perpendicular to the magnetic field detects only fast mode waves. As shown in the figure, we excite acoustic type planar waves at the bottom boundary. This is expected as the vertically directed forcing has the same direction as the magnetic field for most of the bottom boundary. There are small regions near the center (symmetric about $x = 2$) where the magnetic field turns and is not aligned to the vertical direction, causing some disruption of the largely planar wave front structure. Clearly, the velocity in the direction of the magnetic field is symmetric whereas the one in the transverse direction is antisymmetric. Furthermore, the velocity in the transverse direction is strong exactly where the velocity in the direction of the magnetic field is weak.

The waves in the direction of the magnetic field are pushed up vertically whereas the ones in the transverse direction are pushed up sideways. Once the initial wave hits the magnetic canopy ($\beta = 1.2$), the initial acoustic wave mode is converted into a combination of fast and slow mode waves. Note that this mode conversion is taking place in the (horizontal) center of the domain as the magnetic field is strongest here. The resulting waves have an elongated structure as the Alfvén speed is greater than the sound speed in this region.

Then, the waves hit the transition layer and are accelerated due to the increase in sound speed by an order of magnitude as the temperature rises by two orders of magnitude. In particular, the fast waves zoom out of the transition layer with the wave signature visible in the perpendicular component of velocity at time $t = 0.8$. At $t = 1.2$, the velocity in the direction of the magnetic field has a complex structure with rich spatial variation. The magnetic field along the sides, i.e. in the region of $[0, 1] \times [2, 8] \cup [3, 4] \times [2, 8]$ is almost vertical throughout the model, and has little effect on the shape of the waves. The region where the acoustic type waves predominate and the region with a more complex wave structure are clearly delimited in figure 2(c) by the $\beta = 0.1$ isoline. The more complex magnetic field at the base in $x \in [1, 3]$ results in the more complex wave structure in this central region. The fast mode waves are visible in the perpendicular component of velocity and have a compressive saw-tooth like behavior. This compression is also visible in the normal component indicating the formation of shock waves. Furthermore, the waves generated at the center are spreading out. Being fast waves, they can travel across magnetic field lines.

As we are interested in how the waves transport energy from the photosphere into the upper chromosphere and the corona, we consider the relative change in total energy (kinetic + internal + magnetic energy), i.e

$$\mathcal{E}_{i,j}^R(t) := \frac{E_{i,j}(t) - E_{i,j}(0)}{E_{i,j}(0)}.$$

The relative change is a good indicator of how energy is transported. Since we are interested in studying the spatial variation in the energy transfer, the total energy at different horizontal transects is plotted vs. time in figure 3. We choose four different horizontal locations, namely $x = 0.7, 2.0, 2.6, 3.8$. Figure 3 shows a rich spatial variation in the change of energy. At the locations $x = 0.7$ and $x = 3.8$, the basal magnetic field is vertical and quite weak. The energy transport is similar in the two locations. In particular, the original acoustic wave travels up the chromosphere and hits the transition region without much interaction with the magnetic canopy. At the bottom of the transition layer, the wave undergoes both refraction and reflection. A part of the energy is transmitted up into the corona. The refracted wave has a higher speed due to the larger temperature in the corona. A part of the wave energy is also reflected from the transition region and travels down. This wave interacts with the second upward moving incident wave and forms a complex interference pattern. Another part of the wave energy from the first incident wave moves horizontally along the transition layer. The second and third incoming waves have similar behavior but are affected by the waves reflected from the transition layer resulting in interference patterns.

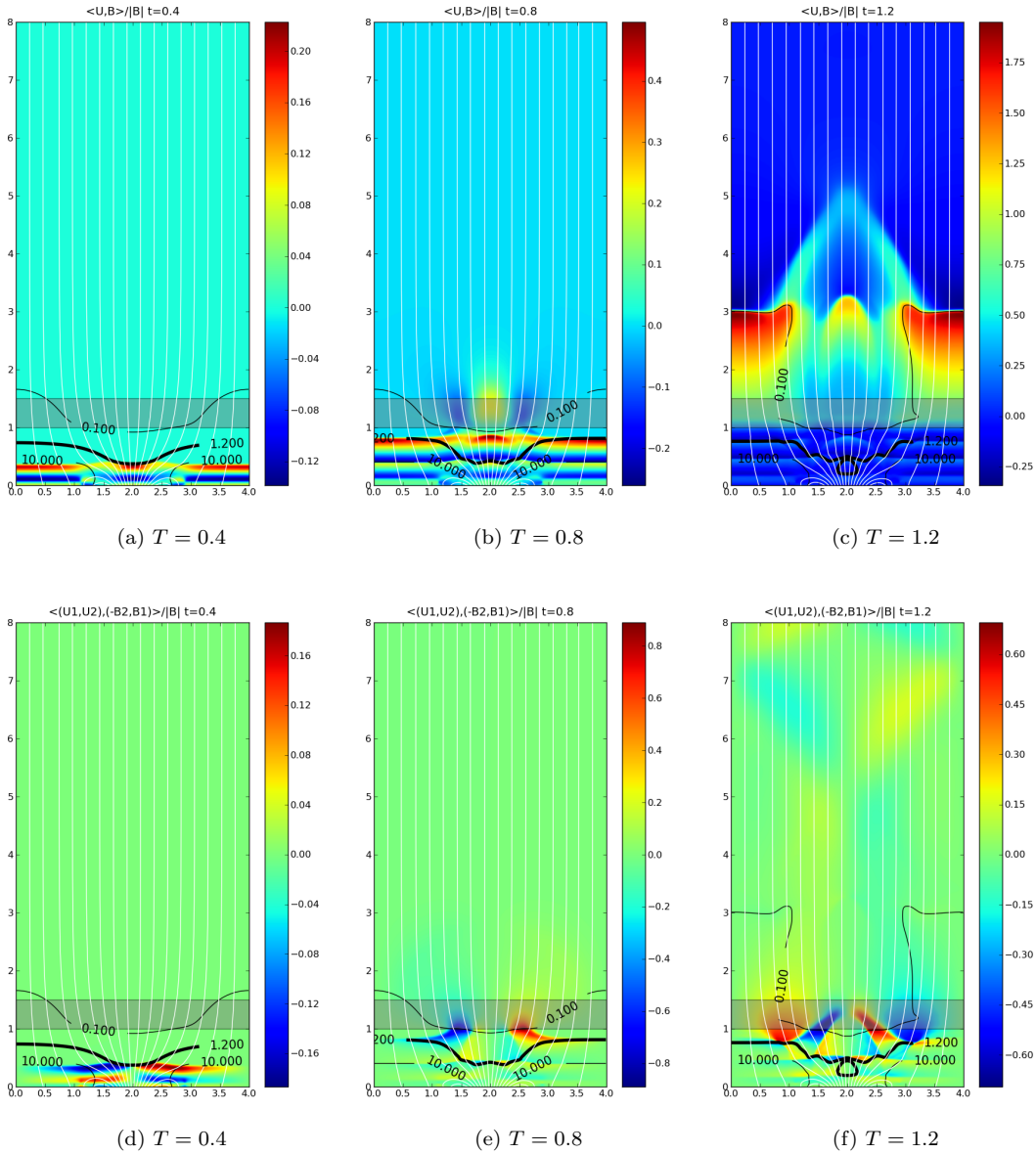


FIGURE 2. Results for the high frequency planar wave experiment. Top: Velocity in the direction of the magnetic field. Bottom: Velocity perpendicular to the direction of the magnetic field. All the results are with a second-order accurate scheme on a mesh of 400×800 points.

At the location $x = 2$, the magnetic field is strong at the bottom. Here, we see a pronounced difference in wave behavior from the previous horizontal locations. In particular, the first incident slow mode wave hits the magnetic canopy and generates fast waves. The fast mode wave is clearly visible at $t = 0.7$. It reaches the transition layer and is accelerated. This wave carries only a very small fraction of the wave energy. The slow mode wave hits the transition region and a part of it is transmitted (refracted) into the corona. A part of the wave energy is also reflected downwards and some of the incident wave energy remains within the transition layer. Notice that the reflected wave interacts with the fast mode excited from the second incident wave at time $t = 1.1$. The waves excited later from the bottom boundary show similar behavior. In this case, the reflection from

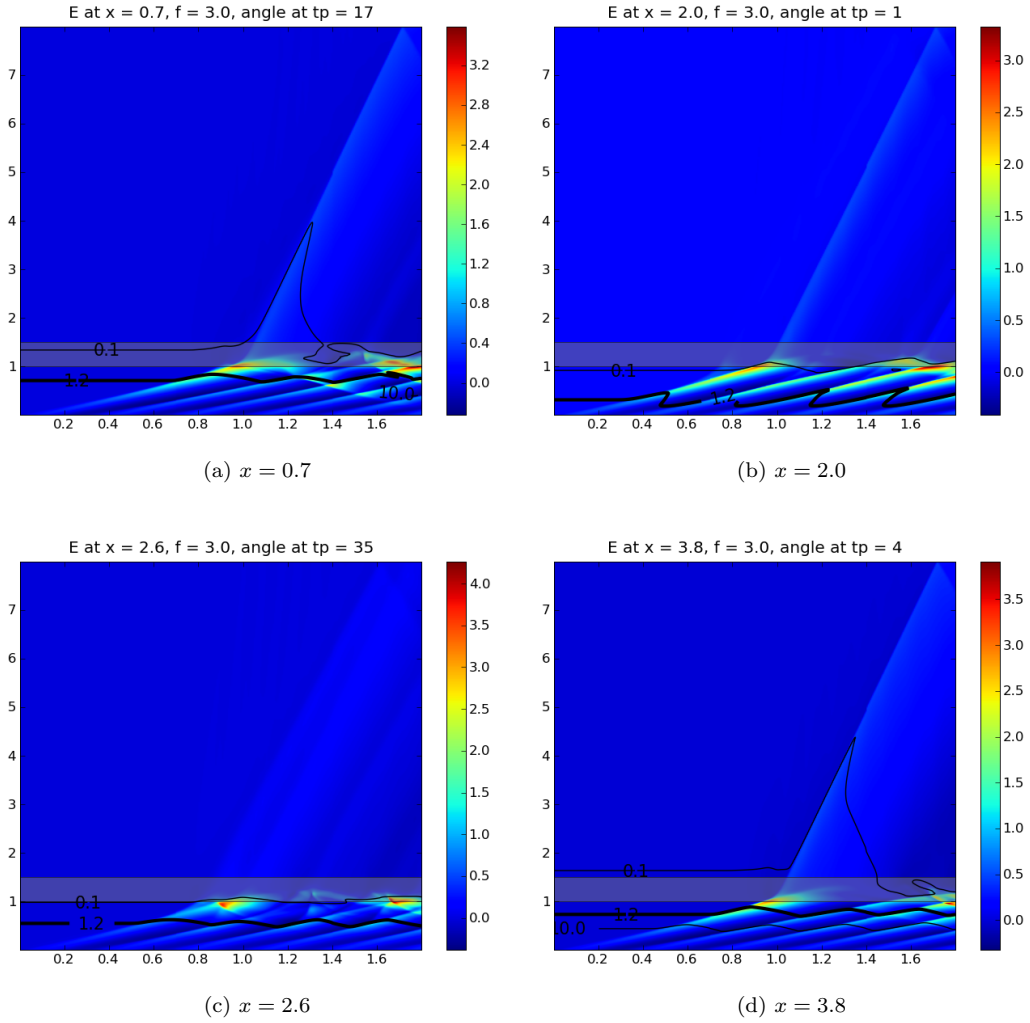


FIGURE 3. Results for the high frequency planar wave experiment. The relative change in total energy as a function of time and height is plotted at different horizontal locations. All the results are with a second-order accurate scheme on a mesh of 400×800 points.

the transition layer appears to be of smaller amplitude than the previous horizontal locations. At the horizontal location $x = 2.6$, the magnetic field is of moderate strength at the bottom and the waves transport energy in a similar manner to the $x = 2$ case. Since the waves hit the canopy at an angle to the magnetic field, we should expect significant mode conversion. Indeed, fast mode waves are clearly excited at the magnetic canopy. Waves are transmitted through the transition layer into the corona. However, a considerable amount of the wave energy remains within the transition region. We observe particularly complicated interference patterns here, which can be attributed to the presence of both mode conversion at the canopy and reflections from the transition region.

Although the waves show rich spatial variation, there are some common features. In particular, the waves carry some of the incident energy into the corona. However, most of the energy is dumped at the base of the transition region and in the upper chromosphere. This is clearly seen in figure 4 where we plot the relative change in energy, integrated across all horizontal locations, in time. This deposition of energy at the base of the transition layer and the chromosphere is a plausible candidate for explaining chromospheric heating.

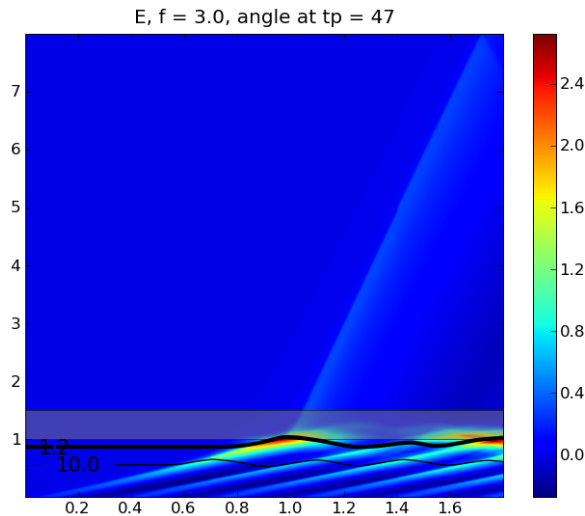


FIGURE 4. Relative change in total energy, integrated across all horizontal locations, vs. time in the high frequency vertical driving case.

4.4. Low frequency planar waves. We change the driving frequency in (4.2) to $\omega = 0.3$. Thus, we drive waves at the photosphere with a frequency which is an order of magnitude less than the previous experiment. The velocities, in directions parallel and perpendicular to the magnetic field are plotted in figure 5. The results are quite similar to the high frequency case (see figure 2 for a comparison). Note that the time levels for the snapshots in the two figures are different.

A key difference with the high frequency excitation lies in how the energy is trapped by the transition region. In order to illustrate this process, we plot the relative change in energy for this case and compare with the high frequency excitation in figure 6. As shown in this figure, there are major differences between both cases. In particular, there is a greater buildup of the energy at the base of the transition region and in the chromosphere for low frequency waves than for high frequency waves. It is not unexpected that more wave energy is trapped, since the frequency of the forcing at the bottom is below the acoustic cut-off of the photosphere. Furthermore, this buildup is spread over a larger portion of the base of the transition region in the low frequency case. This suggests that there will be greater chromospheric heating with low frequency excitations than with high frequency ones.

4.5. Transverse forcing. In the above numerical experiments, the forcing was in the normal direction. In this experiment, we prescribe the transverse driving force,

$$(4.3) \quad \mathbf{u}(x, 0, t) = (0.1 \sin(2\pi\omega t), 0, 0)^T.$$

Here, ω is the driving frequency. We start by considering high frequency excitations at $\omega = 3.0$. The numerical results for this experiment are presented in figures 7,8 and 9. In figure 7, we plot the velocities in the direction of the magnetic field and perpendicular to the magnetic field. There is a clear difference in the wave behavior due to transverse driving from the vertical driving case above. Figure 7 should be compared with figure 2. We excite a combination of fast and slow mode waves at the bottom boundary. The waves in the direction of the magnetic field are anti-symmetric about the $x = 2$ line, whereas those in the direction perpendicular to the field are symmetric about the $x = 2$ line. Unlike the vertical driving, we see that the waves behave as if they are generated by a localized piston, located at the middle of the bottom boundary. There is very little wave excitation in the region where the magnetic field is weak at the bottom, although the forcing acts all across the bottom boundary. The waves move up the chromosphere and hit the magnetic canopy where mode conversion takes place. The waves are accelerated when they hit the transition layer. The resulting waves have a semi-circular arch shape and have a pronounced sideways turning motion, which should be contrasted with the vertical driving case.

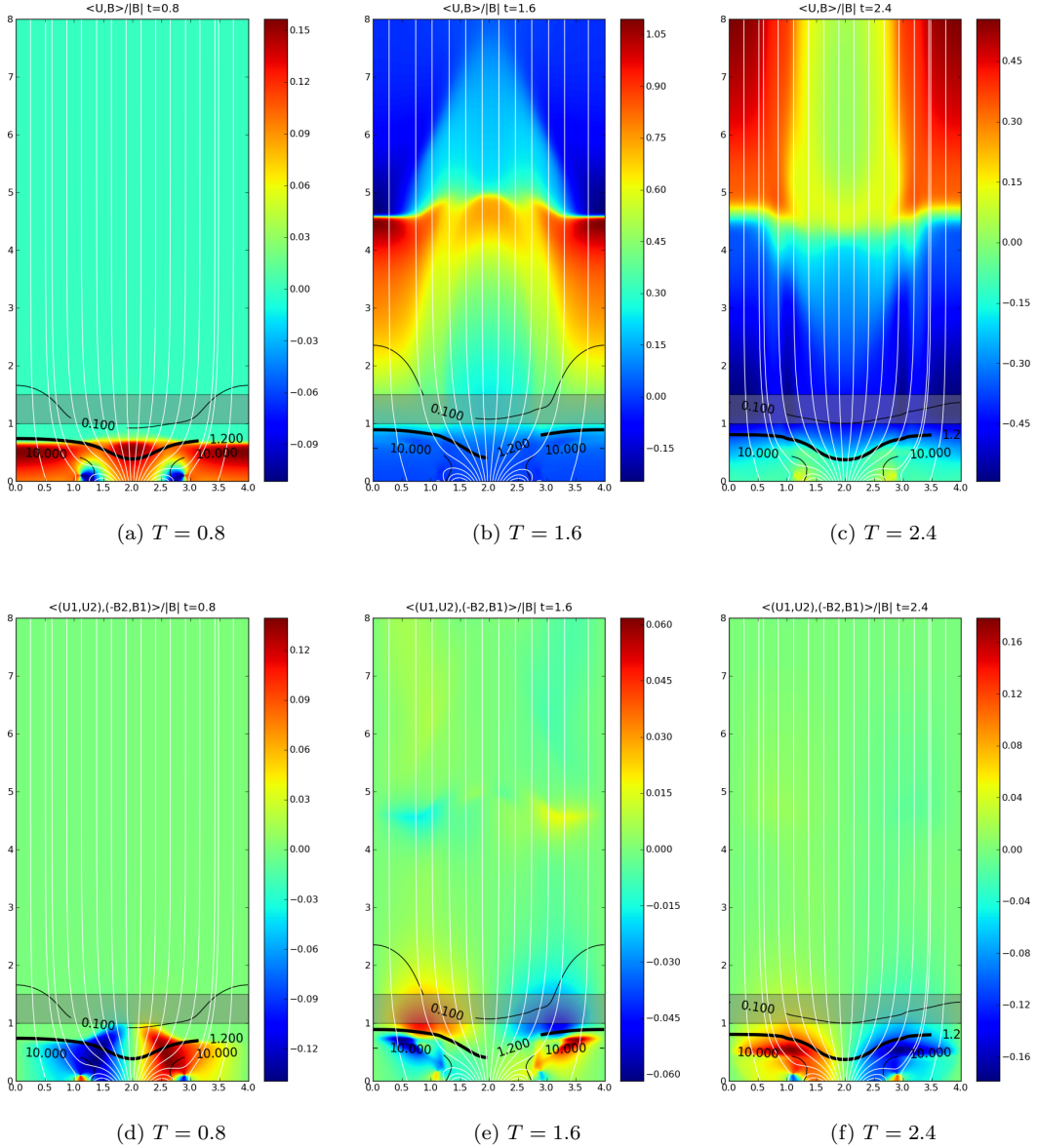


FIGURE 5. Results for the low frequency planar wave experiment. Top: Velocity in the direction of the magnetic field. Bottom: Velocity perpendicular to the direction of the magnetic field. All the results are with a second-order accurate scheme on a mesh of 400×800 points.

The relative energy change (as a function of time and height) at four different horizontal locations $x = 0.7, 2.0, 2.6, 3.8$ is shown in figure 8. Again, there are considerable differences between this example and the one with vertical driving. In particular, the amplitude of energy gains at all four locations is considerably smaller in this case (compare with figure 3). Furthermore, a much larger proportion of the energy leaks into the corona. There is again a rich spatial variation in the energy transfer. At $x = 2$, the magnetic field is strong at the bottom and the initial waves are acoustic type waves. Fast mode waves are also generated when the incident waves hit the magnetic canopy. These fast waves are transmitted into the corona. As the slow wave hits the transition region, a part of the energy is reflected. Notice that the reflections have lower amplitude in this

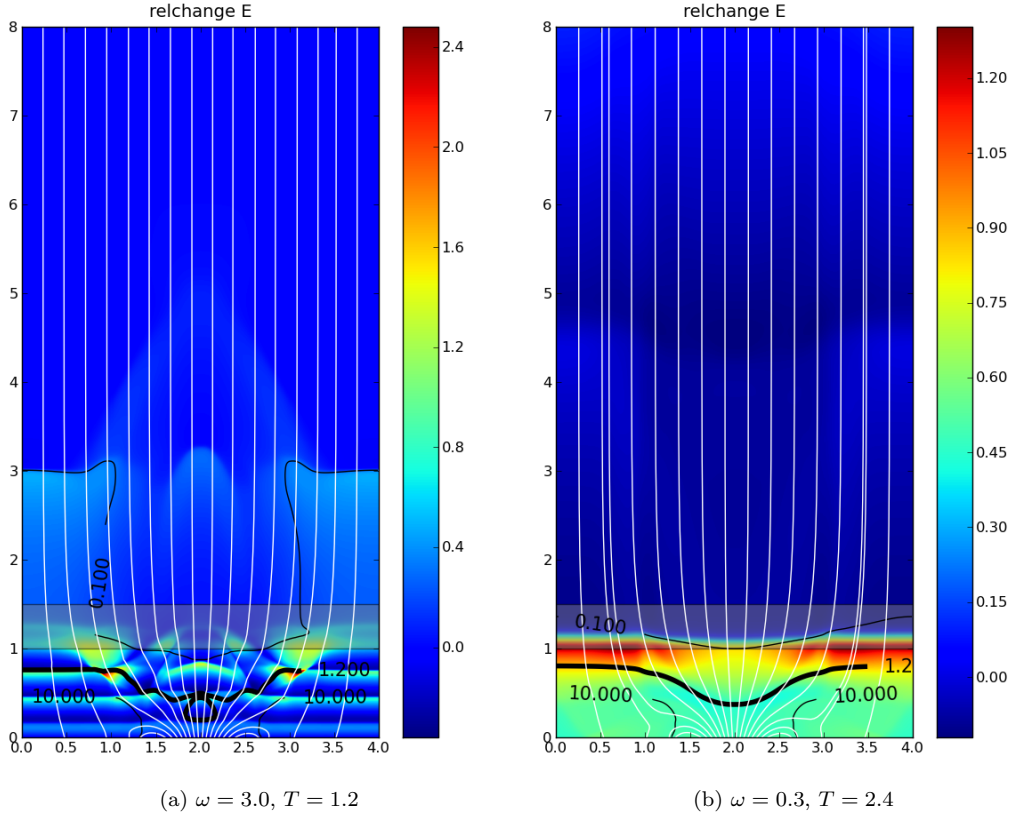


FIGURE 6. A comparison of the relative change in energy for the high frequency case and the low frequency case. Both results are for the vertical driving at comparable times.

case than the one with vertical forcing. Furthermore, some of the wave energy remains within the transition layer. The trailing waves interact with the reflected waves and horizontal waves in the transition layer, forming a complex pattern. A similar qualitative behavior is encountered at the spatial location $x = 2.6$. The main difference with the previous location lies in the fact that fewer fast waves are excited. At $x = 0.7$, the magnetic field is approximately zero at the bottom $z = 0$. There are few visible fast waves and most of the energy is carried by slow mode waves. A large fraction of the waves seen around the $\beta = 1.2$ isoline after time $t \approx 1.2$, are waves generated around the center, entering from the side, compare figure 10. They interact with upward moving waves forming a complex interference pattern. At the location $x = 3.8$, the magnetic field is again close to zero at the bottom boundary and we see a similar behavior to the case $x = 0.7$. A large proportion of the incident wave energy is transmitted into the corona. The relative change, integrated in the horizontal direction, (as a function of time) is shown in figure 9. It highlights the differences with the vertical driving case (figure 4). The amplitude of energy change is smaller in this case but a larger proportion of the wave energy leaks into the corona.

We repeated the simulations with the driving (4.3) but with frequency $\omega = 0.3$. The wave dynamics for this low frequency case was very similar to the one with high frequency excitations. The main difference in the relative change in energy is shown in figure 10. As in the vertical driving case, the low frequency excitations result in a greater buildup of energy at the base of the transition region and in the chromosphere.

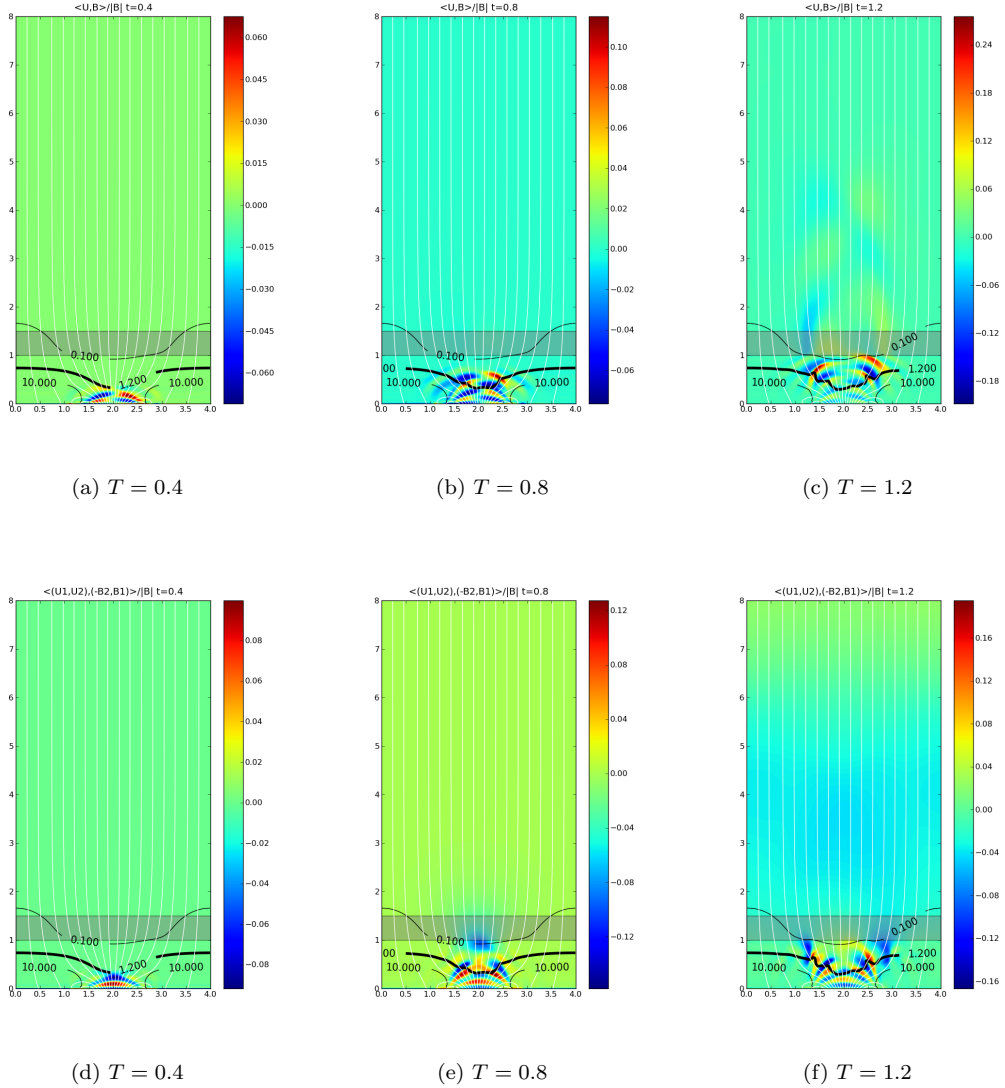


FIGURE 7. Results for the high frequency planar wave experiment with driving (4.3). Top: Velocity in the direction of the magnetic field. Bottom: Velocity perpendicular to the direction of the magnetic field. All the results are with a second-order accurate scheme on a mesh of 400×800 points.

5. NUMERICAL RESULTS IN THREE SPACE DIMENSIONS

In this section, we will present numerical results for wave propagation in a three dimensional model solar atmosphere. The temperature profile is exactly the same as in the previous section.

5.1. Synthetic magnetic field. To begin with, we consider a synthetic background magnetic field of the following form. Let

$$(5.1) \quad B_3(x, y, 0) = 0.0275 \left(2.8e^{-6.4r^2} - 0.7e^{-40(r-0.75)^2} \right), \quad x, y \in [0, 4], r = \sqrt{(x-2)^2 + (y-2)^2}.$$

In 3d we take the zeroth component of the Fourier term (2.10) 4 times, i.e. $\tilde{a}_{0,0} = 4a_{0,0}$. The magnetic field is constructed from the first 16×16 Fourier co-efficients. The computational domain

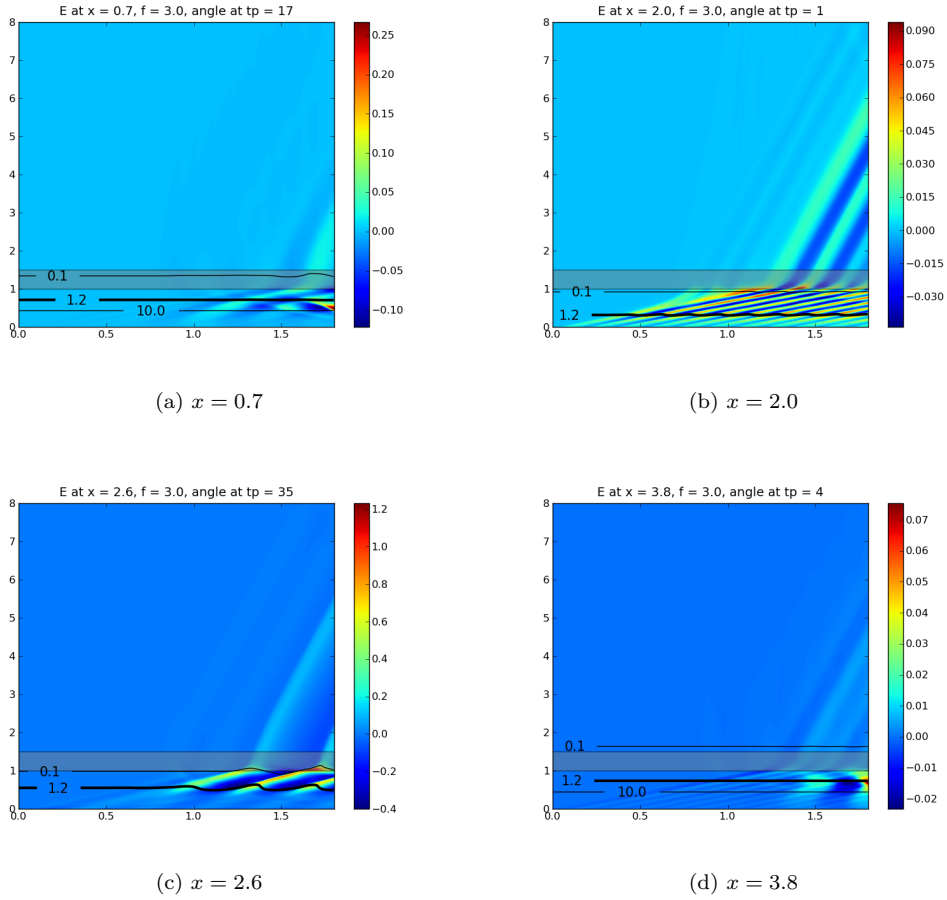


FIGURE 8. Results for the high frequency planar wave experiment with transverse driving (4.3). The relative change in total energy as a function of time and height is plotted at different horizontal locations, characterized by different attack angles. All the results are with a second-order accurate scheme on a mesh of 400×800 points.

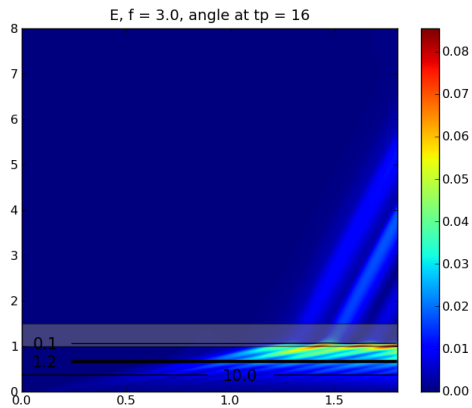


FIGURE 9. Relative change in total energy, integrated across all horizontal locations, vs. time in the 2-D transverse driving case.

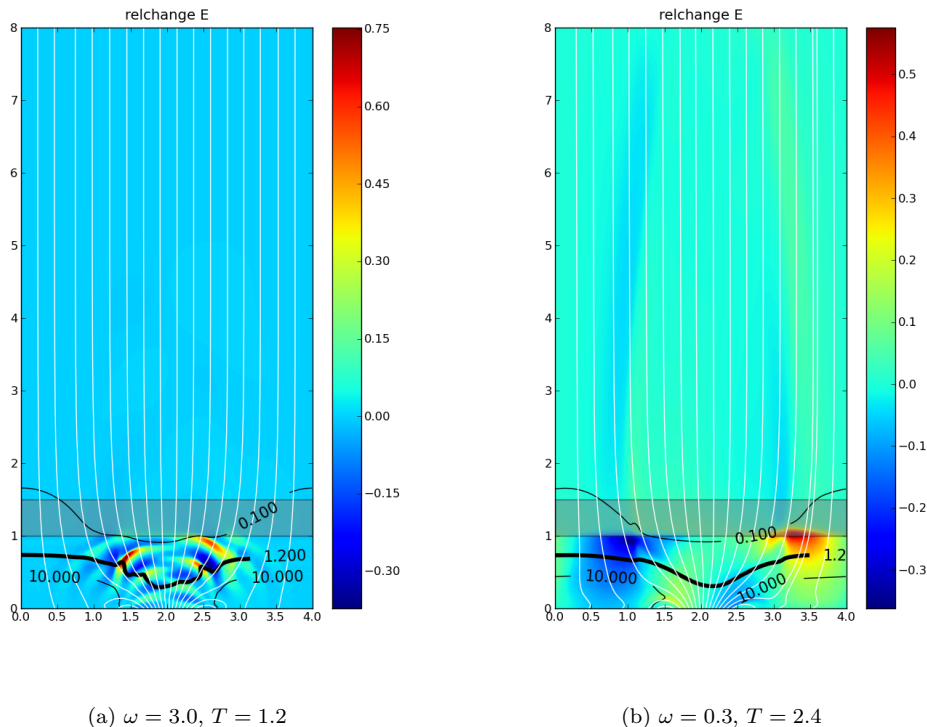


FIGURE 10. A comparison of the relative change in energy for the the high frequency case and the low frequency case. Both results are for transverse driving at comparable times.

is $(x, y, z) \in [0, 4] \times [0, 4] \times [0, 8]$ and the parameters g, H and p_0 are the same as in the previous section. Figure 11 shows the field lines of the background magnetic field in white and the magnetic field strength at $z = 0$. Furthermore, the blue isosurface is the location of the magnetic canopy, i.e. $\beta = 1.2$.

5.1.1. *Planar waves with vertical forcing.* We excite planar waves at the bottom boundary with the forcing,

$$(5.2) \quad \mathbf{u}(x, y, 0, t) = (0, 0, 0.1 \sin(2\pi\omega t))^T,$$

with the frequency ω set to 3. The results of this experiment are presented in figures 12, 13 and 14. As there are three directions, we follow Carlsson and Bogdan (2006) and show the velocity in the direction of the magnetic field as well as in two perpendicular transverse directions to the magnetic field. These two directions are calculated as in Carlsson and Bogdan (2006) and are termed as the principal normal direction and the binormal direction. This decomposition of the velocity field serves to investigate the existence of two transverse wave modes.

We show isosurfaces of the velocity field in all the three directions in figure 12. The figure shows that there is a marked difference between velocity in the normal direction and in the two transverse directions. In particular, the velocity in the normal direction shows waves that are excited all over the domain, including at the edges where the magnetic field is quite weak at the bottom. On the other hand, the transverse waves are present only in the center of the domain where the basal magnetic field is strong. This is similar to the two dimensional situation. The two transverse wave modes are quite different from each other. The mode illustrated by the principal normal direction has a four fold (quadrant) symmetry whereas the waves in the binormal direction

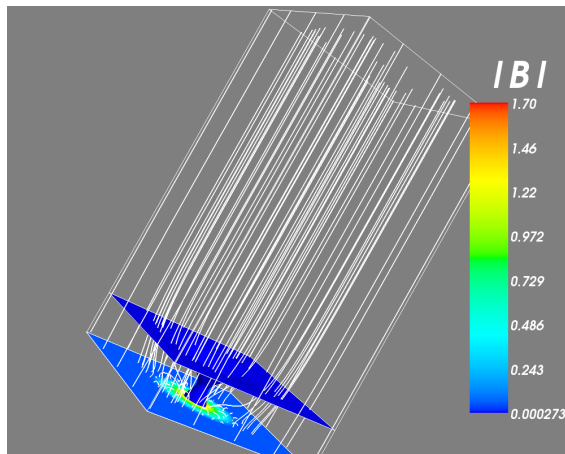


FIGURE 11. Background magnetic field in 3 dimensions. The magnetic field lines are shown in white. At $z = 0$ we show the strength of the magnetic field. The points where $\beta = 1.2$ lie on the blue isosurface.

have a (approximately) radial symmetry. These differences in the two transverse directions may indicate the existence of two different transverse wave modes (Carlsson & Bogdan 2006). We will examine this issue in some detail later in this section.

The relative change in total energy as function of time and at four different horizontal locations is shown in figure 13. The figures show pronounced spatial variation in how the waves transport energy up the solar atmosphere. At the location $(2.0, 2.0)$, i.e the center of the horizontal domain, the magnetic field is strong at the bottom. Here, we see that the initial acoustic waves carry energy up the chromosphere. The magnetic field is strong enough that the waves do not intersect the iso-surface $\beta = 1.2$ at this location. Consequently, there are no visible signs of mode conversion. The waves hit the transition layer and a part of the wave energy is transmitted (refracted) into the corona. These waves are accelerated at the transition region. There is little evidence of reflections from the transition region in the figure. This phenomenon could well be explained by the reflected waves traveling along some other direction and therefore not being visible at the location $(2.0, 2.0)$. Still, a large proportion of the wave energy is dumped at the base of the transition region. Very similar wave dynamics is observed at the locations $(2.25, 2.0)$ and $(2.2, 2.2)$ where the magnetic field is moderately strong at the bottom. At the location, $(3.9, 3.9)$, the magnetic field is close to zero at the bottom. Although the incident waves cross the magnetic canopy, there is little evidence for mode conversion.

The relative change in energy (as a function of time), integrated across all horizontal locations, is presented in figure 14. It reinforces the conclusion that although some part of the wave energy is transmitted to the corona, a bulk of the wave energy is deposited in the chromosphere and at the base of the transition region. This observation is similar to the two dimensional case.

In three dimensions, it is expected that Alfvén waves are either excited at the bottom boundary or are generated by mode conversion. We need to examine the numerical results carefully in order to investigate the presence of Alfvén waves. In Carlsson and Bogdan (2006), the authors proposed that differences in the wave structure along the principal normal and binormal directions to the magnetic field indicates the presence of two different transverse wave modes. This provides some indirect evidence for the existence of Alfvén waves. From figure 12, we clearly observe that the waves along the two transverse directions are different. Does this indicate the presence of Alfvén waves? In order to investigate this issue further, we plot the relative change in pressure and the velocity components parallel, in the principal normal and binormal directions to the magnetic field in figure 15. All the plots are at time $t = 1.4$ and we show the views from the top of the domain as well as from the side in figure 15. It is well known that the pressure should not change across an Alfvén wave whereas both fast and slow mode waves change the pressure. A comparison

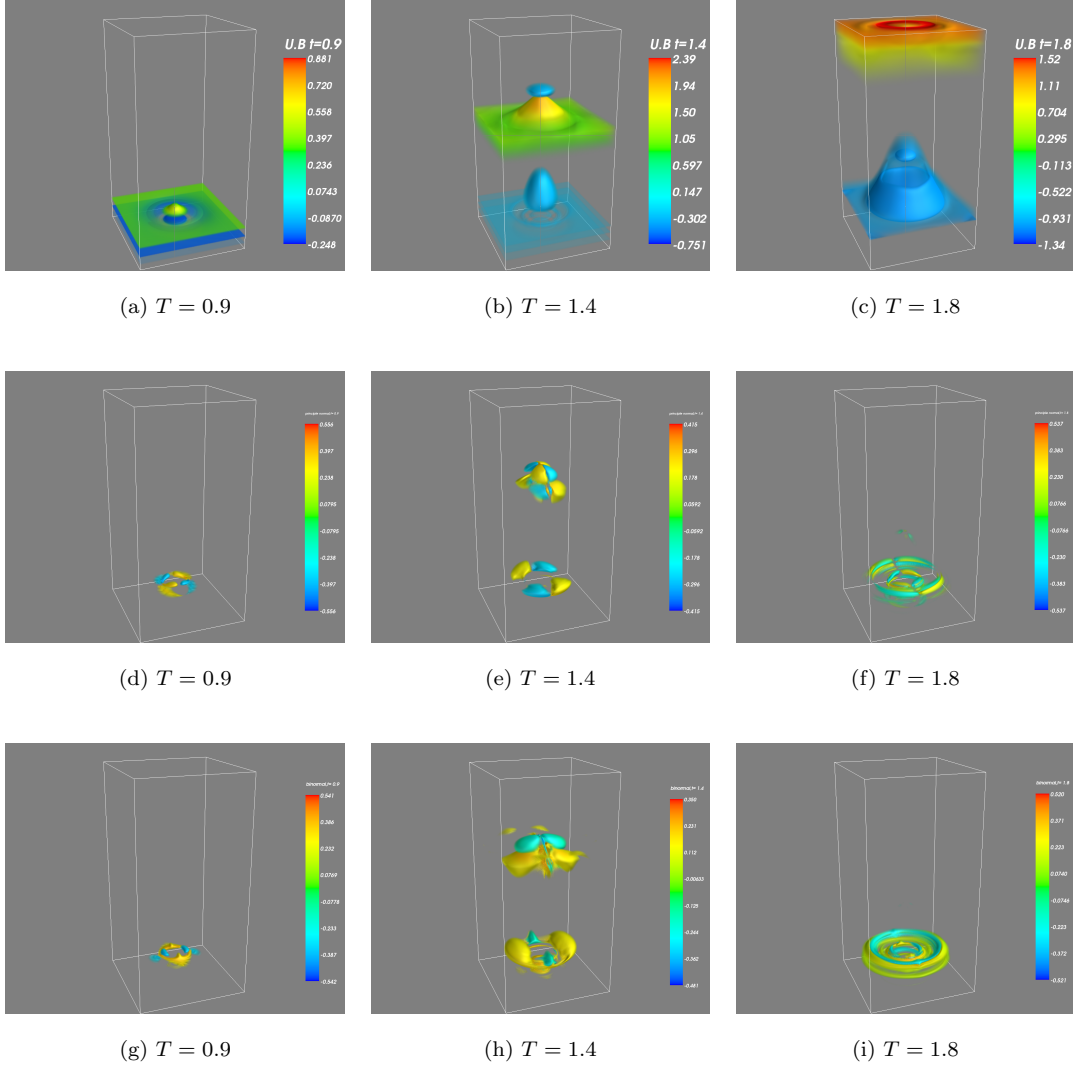


FIGURE 12. Results for the 3-D high frequency planar wave experiment with synthetic magnetic field and driving (5.2). Top: Velocity in the direction of the magnetic field. Middle: Velocity in the principal normal direction. Bottom: Velocity in the binormal direction to the magnetic field. All the results are with a second-order accurate scheme on a mesh of $400 \times 400 \times 800$ points.

of the relative change in the pressure and the velocity along the magnetic field shows that the pressure jump is correlated to the velocity along the field for most of the domain. These waves are a combination of fast and slow modes. In the region where there is no evidence for waves in the direction of the magnetic field, the pressure jump seems to be caused by a combination of the two transverse wave modes. This indicates that both modes are probably (combinations of) fast waves and there is no direct evidence for the existence of coronal Alfvén waves in this particular case.

5.1.2. *Transverse driving.* We consider the same configuration as in the previous numerical experiment but prescribe the transverse driving

$$(5.3) \quad \mathbf{u} = -0.1(\cos(2\pi\omega t), \sin(2\pi\omega t), 0)^T, \mathbf{B} = 0.1(\cos(2\pi\omega t), \sin(2\pi\omega t), 0)^T.$$

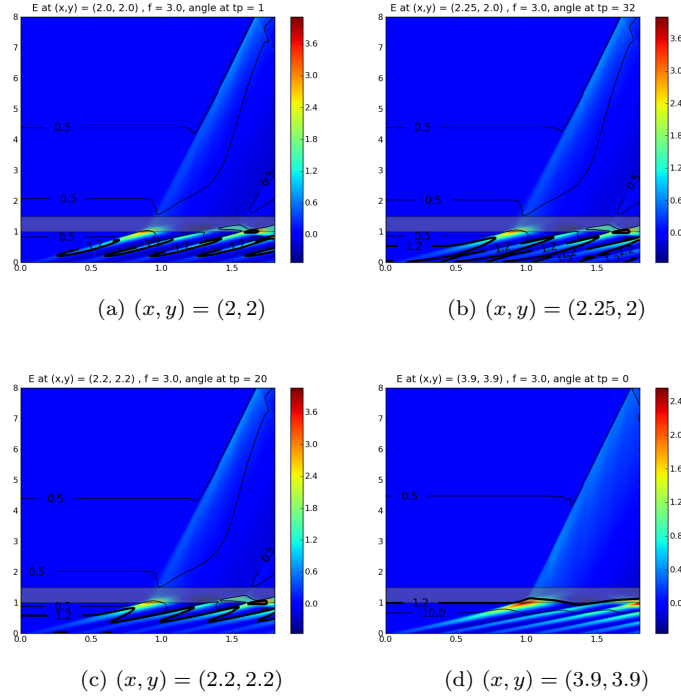


FIGURE 13. Relative change in total energy (as a function of height and time) at four different horizontal locations in the high frequency planar wave experiment with synthetic magnetic field and driving (5.2). All the results are with a second-order accurate scheme on a mesh of $400 \times 400 \times 800$ points.

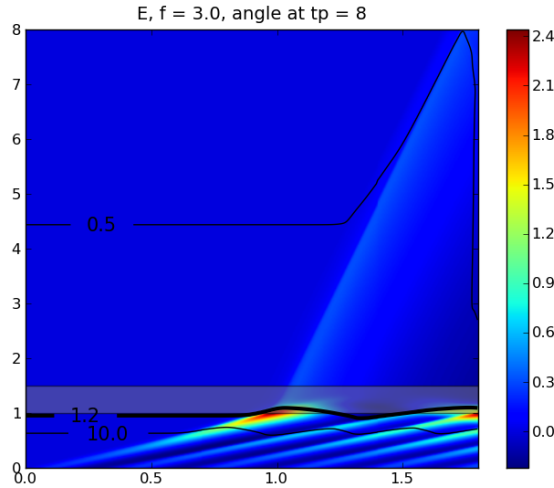


FIGURE 14. Relative change in total energy, integrated across all horizontal locations, vs. time in the 3-D vertical driving case.

The frequency $\omega = 3.0$ is considered and the results are shown in figures 16 - 19. In figure 16, we show waves along the magnetic field and in the principal normal and binormal directions to the magnetic field. As the forcing is transverse, we are exciting waves horizontally. In this case, the shape and structure of the waves is very different from that of the vertical driving case, compare with figure 12. The waves in the direction of the magnetic field have a *spiral* motion along the

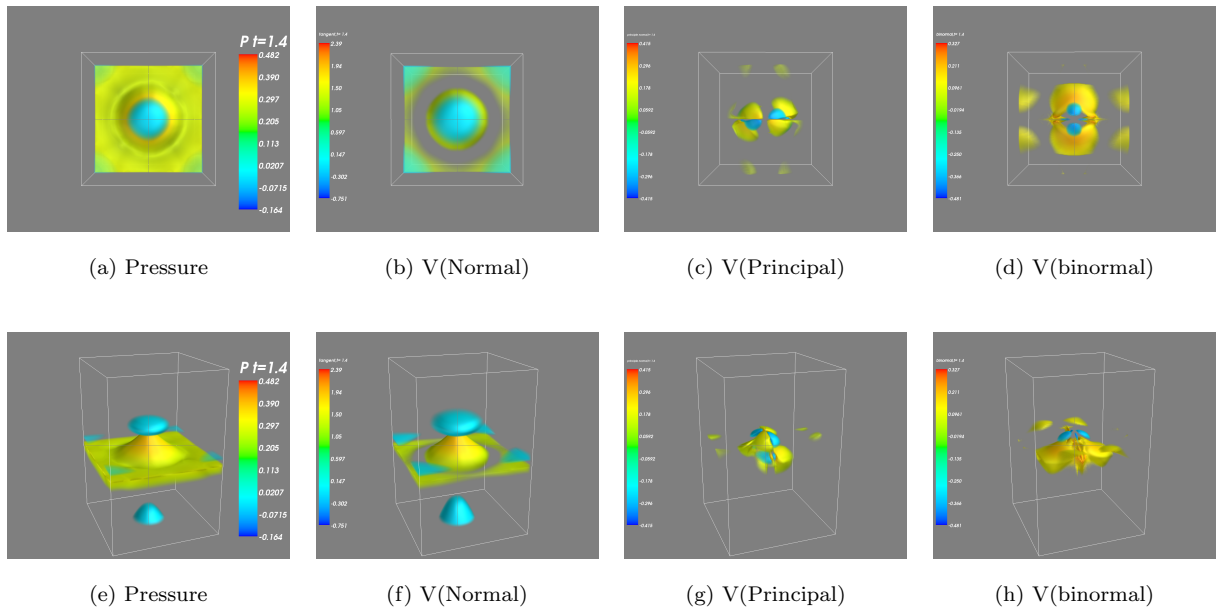


FIGURE 15. Results for the high frequency planar wave experiment with synthetic magnetic field and driving (5.2). We show change in pressure and velocities in the three orthogonal directions at time $t = 1.4$. Top: View down the top boundary. Bottom: Side view. All the results are with a second-order accurate scheme on a mesh of $400 \times 400 \times 800$ points.

magnetic field. The magnetic field is at its strongest at the center of the domain and we see that the waves spiral around this central region. On the other hand, the waves in the two transverse directions have a directed upward motion in the center of the domain. As in the two-dimensional case, transverse forcing seems to act like a localized piston sending out waves from the middle of the bottom boundary, where magnetic field is concentrated.

There is a clear evidence of mode separation once the waves have crossed the transition layer into the corona. As seen in figure 16 (at time $t = 1.4$), the spiral waves in the direction of the magnetic field are clearly slow mode waves. On the other hand, waves in the transverse directions are much faster. Near the top boundary, the fast and Alfvén waves travel at the same speed. So, it is unclear whether the transverse waves are fast mode waves or Alfvén waves. We examine this issue in figure 17 where the relative change in pressure is plotted along with the velocities in all three orthogonal directions. Figure 17 clearly shows that the pressure jump is completely correlated with the slow mode wave. On the other hand, waves in both transverse directions do not have any pressure change across them. This is a clear signature of Alfvén waves. Furthermore, these transverse waves are constricted by the strong magnetic field which is another characteristic of Alfvén waves as fast mode waves can spread out across the magnetic field. Together, these observations provide fairly strong direct evidence for the presence of Alfvén waves in this configuration.

The energy carried by waves (as a function of time) at four different horizontal locations is shown in figure 18. There are marked differences in the energy landscape at different horizontal locations. At the middle of the domain $(x, y) = (2, 2)$, the magnetic field is quite strong at the bottom and the incident waves do not intersect the magnetic canopy. The incident wave energy is mostly accumulated in the chromosphere and at the base of the transition region. Some of the wave energy is transmitted into the corona. Significant wave energy is trapped within the transition layer, creating what appears like a standing wave. Trailing incident waves interact with this trapped energy and are unable to transmit wave energy into the corona. The energy landscape at the locations $(2.2, 2.2)$ and $(2.25, 2)$ is quite similar. These locations have a background magnetic

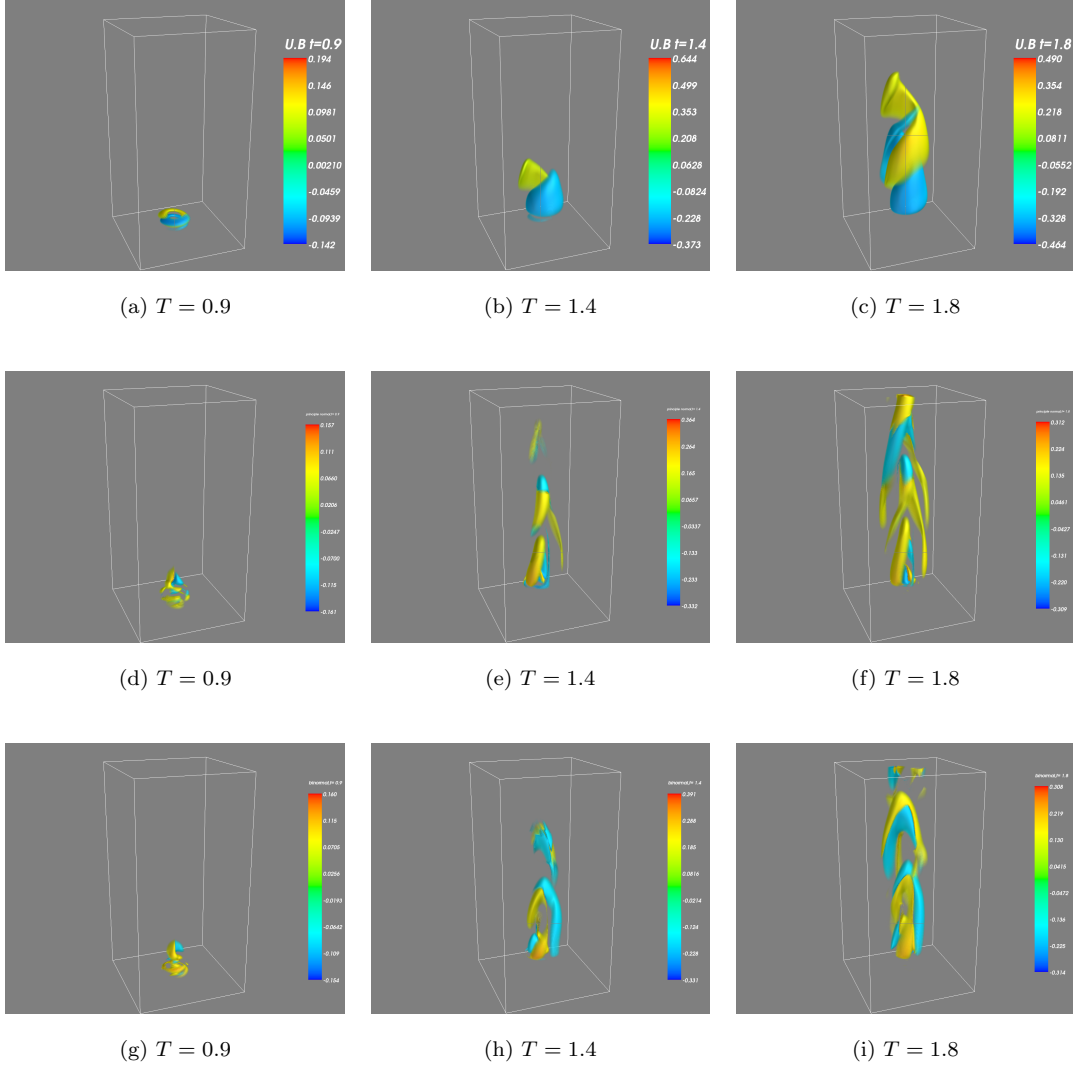


FIGURE 16. Results for the three dimensional high frequency planar wave experiment with synthetic magnetic field and transverse driving (5.3). Top: Velocity in the direction of the magnetic field. Middle: Velocity in the principal normal direction. Bottom: Velocity in the binormal direction to the magnetic field. All the results are with a second-order accurate scheme on a mesh of $400 \times 400 \times 800$ points.

field that is of moderate strength at the bottom. In this case, there is evidence of low energy waves in the corona that are faster than the incident waves. We believe that these are signatures of the Alfvén waves. A much larger proportion of the wave energy is transmitted into the corona at these locations compared to other horizontal locations. At the location $(3.9, 3.9)$, there are very small amplitude waves as the magnetic field is really weak at the bottom. A considerable part of the incident wave energy is reflected from the transition layer in this case. The relative energy change (integrated across all horizontal locations) is shown in figure 19. It shows that most of the energy is accumulated at the upper chromosphere while a small proportion of it is transmitted into the corona. The main difference with the vertical driving lies in the amplitude of the energy change and in the fact that a greater proportion of energy is transmitted into the corona.

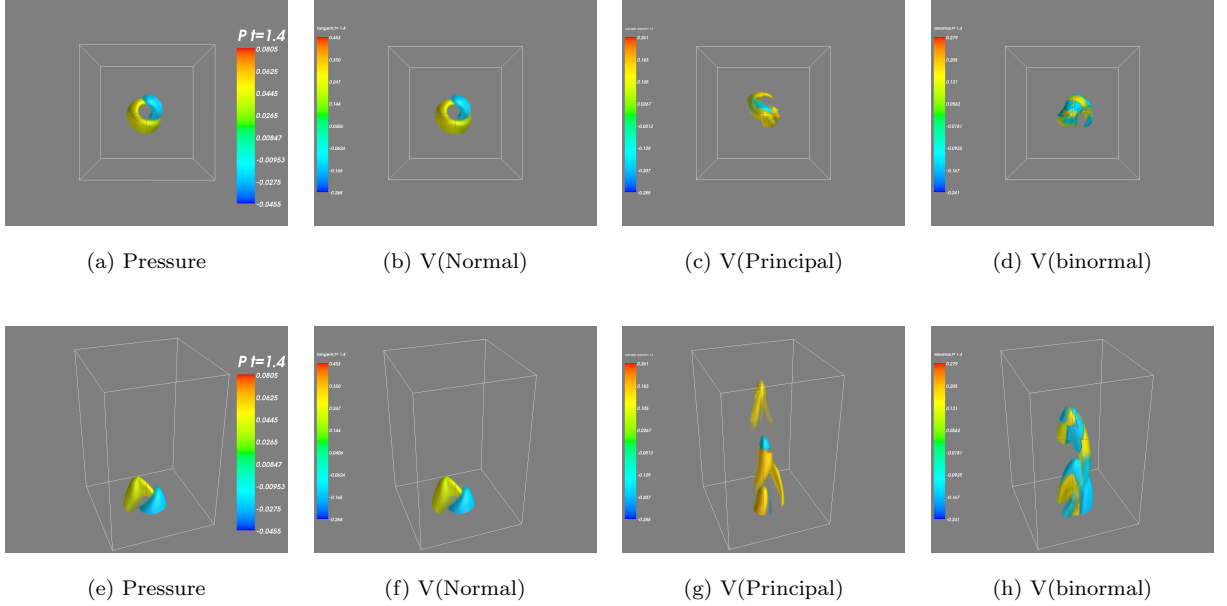


FIGURE 17. Results for the high frequency planar wave experiment with synthetic magnetic field and transverse driving (5.3). Top: Velocity in the direction of the magnetic field. Middle: Velocity in the principal normal direction. Bottom: Velocity in the binormal direction to the magnetic field. All the results are with a second-order accurate scheme on a mesh of $400 \times 400 \times 800$ points.

5.2. Observed magnetic field. The above numerical experiments were performed with synthetic magnetic fields and bottom boundary conditions. The real test of a code like SURYA is its performance on observed data sets. For this purpose, we present a three-dimensional simulation of the solar atmosphere with the same temperature profile as in the previous numerical experiments. The background magnetic field $\tilde{\mathbf{B}}$ is given by (2.10) where the Fourier coefficients are extracted from the magnetic field at the bottom boundary. Using the 3d data model of Carlsson and Stein (2002), measurements of the solar radial magnetic field by the MDI instrument on SOHO in 1997 are used to obtain the magnetic field at the bottom boundary. This *observed* background field is depicted in figure 20. It is very complex with a rather chaotic combination of open and closed loop field lines.

5.2.1. Observed driving. We excite waves at the bottom boundary by using a forcing that was observed in the same part of the solar surface by SOHO and at the same time as the background magnetic field. The results of this simulation with observed magnetic field and observed driving are shown in figures 21, 22 and 23.

In figure 21, we plot the velocities in the direction of the magnetic field and in the principal normal and binormal directions to the magnetic field. The results show very complicated wave behavior. There are strong differences between waves in the three directions. No obvious symmetries are seen in the plot. This could be attributed to the nature of the forcing which will contain a combination of vertical and transverse driving motions.

It is simpler to analyze the energy carried by waves. We plot the relative change in energy at four different horizontal locations. There is a very complex spatial variation in the energy transfer. At the location (7.6, 2.3), the magnetic field is very weak. Here the incident waves carry energy up to the transition region. Most of the energy is dumped at the base of the transition region, and only a small part of the wave energy is transmitted into the corona. At the location (5.3, 8.4), the magnetic field is stronger at the bottom compared to the previous location. Here, there is evidence

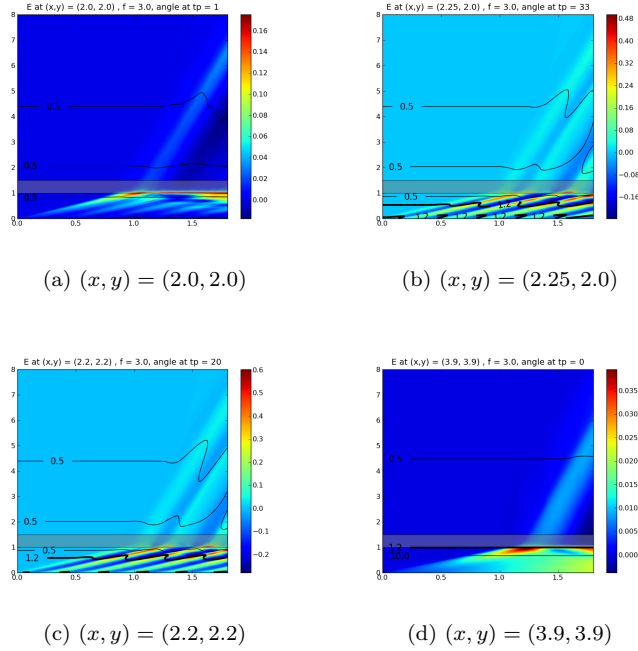


FIGURE 18. Relative change in total energy (as a function of height and time) at four different horizontal locations in the three dimensional high frequency planar wave experiment with synthetic magnetic field and driving (5.3). All the results are with a second-order accurate scheme on a mesh of $400 \times 400 \times 800$ points.

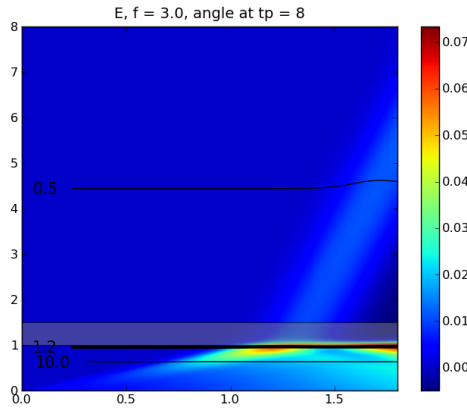


FIGURE 19. Relative change in total energy, integrated across all horizontal locations, vs. time in the 3-D transverse driving case.

for fast wave modes in the corona. However, these waves carry a small amount of energy. Most of the wave energy is contained in incident waves that dump it in the chromosphere. Some of this energy is also transmitted into the corona. The magnetic field is even stronger at the the bottom of the location (17.5, 12.2). Here, there is considerable evidence of fast waves in the corona. A larger proportion of the wave energy is transmitted into the corona. At this location, there is a constant forcing at the photospheric boundary, but only a small part of the wave propagates upwards. This could very well be the result of the magnetic field that is almost horizontal at this

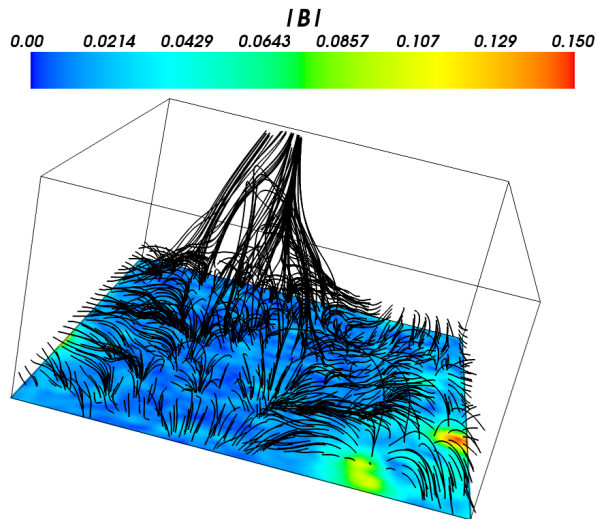


FIGURE 20. The background magnetic field for simulations with observed data.

point. The behavior at the location (14.5, 16.8) is similar. There are a large number of low energy waves in the corona. There is energy accumulation at the base of the transition region at later times at this location.

Although the detailed spatial picture for energy transfer by waves is quite complicated, the gross (integrated across horizontal locations) change in energy is very similar to that of the synthetic magnetic fields. We plot this integrated relative energy change (as a function of time) in figure 23. The figure shows that the detailed wave dynamics cancel out in the mean and the main features are the deposition of a bulk of the wave energy in the chromosphere with a smaller proportion of the energy leaking into the corona.

6. CONCLUSION

We simulate waves in the solar atmosphere using SURYA. This code is based on solving the equations of stratified MHD (2.1) using a recently developed high-order well-balanced finite volume scheme. The code uses stable finite volume schemes resulting from an upwind discretization of the Godunov-Powell source terms for the ideal MHD equations. It is able to handle two and three dimensional configurations with diverse background magnetic fields and driving mechanisms, including observed data sets.

We employ SURYA to perform simulations of waves in various configurations. In two space dimensions, we performed simulations with a complex synthetic magnetic field and observe that

- The behavior of waves strongly depends on the directionality of the forcing. For vertical planar forcing, the waves in the direction of the magnetic field are excited over the entire domain whereas transverse waves are only excited in regions of strong magnetic field. On the other hand, when we force the transverse component, both normal as well as transverse waves are excited only in regions of strong magnetic field. In the transverse forcing case, the driving takes the form of a localized piston at concentrations of the magnetic field.
- There is mode conversion at the magnetic canopy ($\beta = 1.2$), particularly in regions of strong magnetic field. Fast waves are generally excited at the canopy. Furthermore, the transition layer serves to accelerate the waves on account of the increase in sound speed as the temperature increases in the corona. Hence, there is a complex co-existence of fast and slow mode waves in the corona.
- For both types of forcing, waves are transmitted into the corona although there are reflections from the base of the transition layer. Furthermore, waves that travel horizontally along the transition layer are also excited.

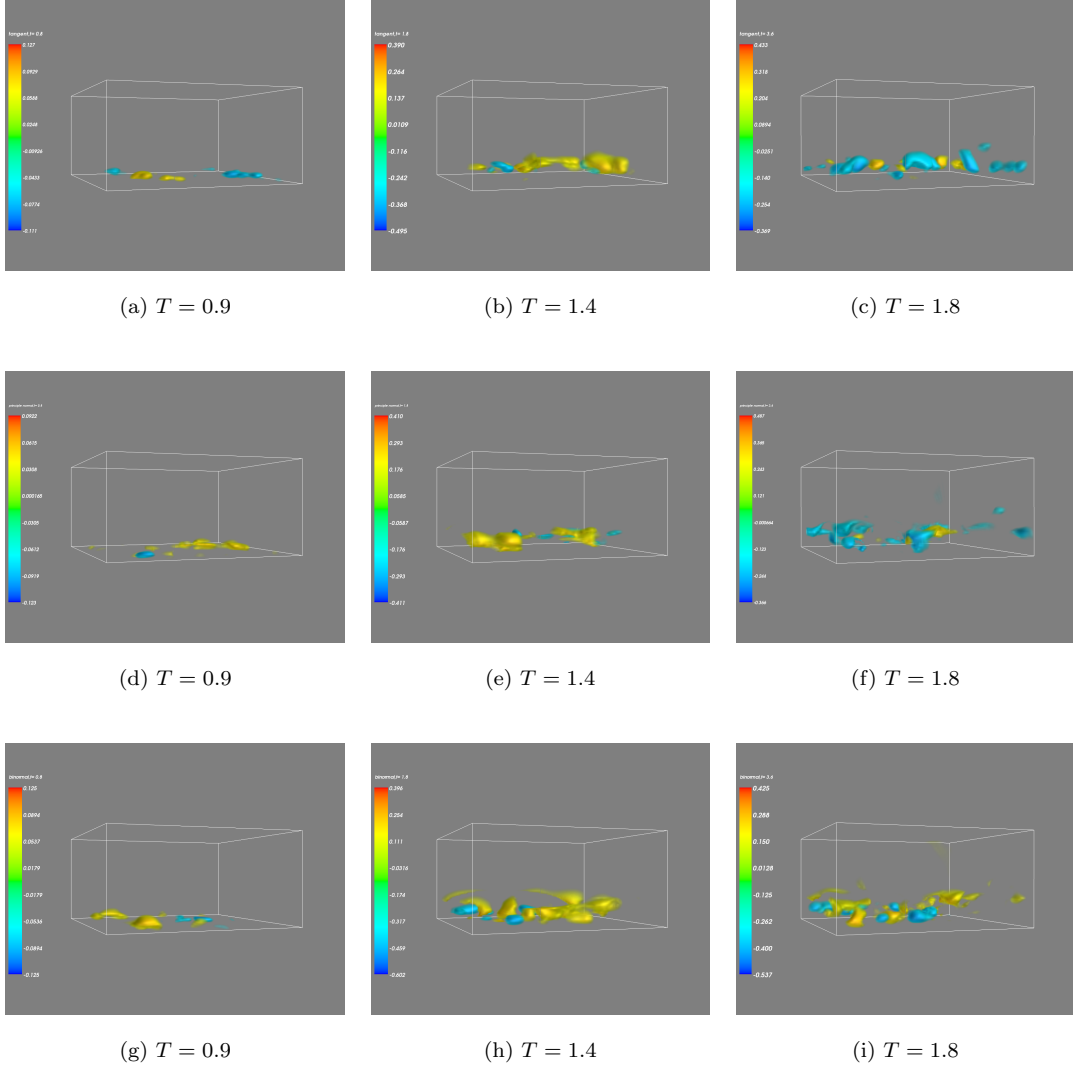


FIGURE 21. Results for the three dimensional experiment with observed magnetic field and driving. Top: Velocity in the direction of the magnetic field. Middle: Velocity in the principal normal direction. Bottom: Velocity in the binormal direction to the magnetic field. All the results are with a second-order accurate scheme on a mesh of $120 \times 120 \times 60$ points.

- There is a rich spatial variation in the energy transferred by the waves. The energy transfer is strongly dependent on magnetic field strength compared to the pressure at a given location.
- For both types of forcing, most of the wave energy (carried by incident acoustic waves) is dumped in the chromosphere and at the base of the transition layer. Some of it is reflected down the chromosphere and a smaller proportion is transmitted into the corona. The main difference between the planar and transverse forcing seems to lie in the fact that a greater proportion of the energy is transmitted in the transverse forcing case.
- The dynamic behavior of the waves and the details of energy transfer through waves is less dependent on the forcing frequency. But we observe that in the low frequency case,

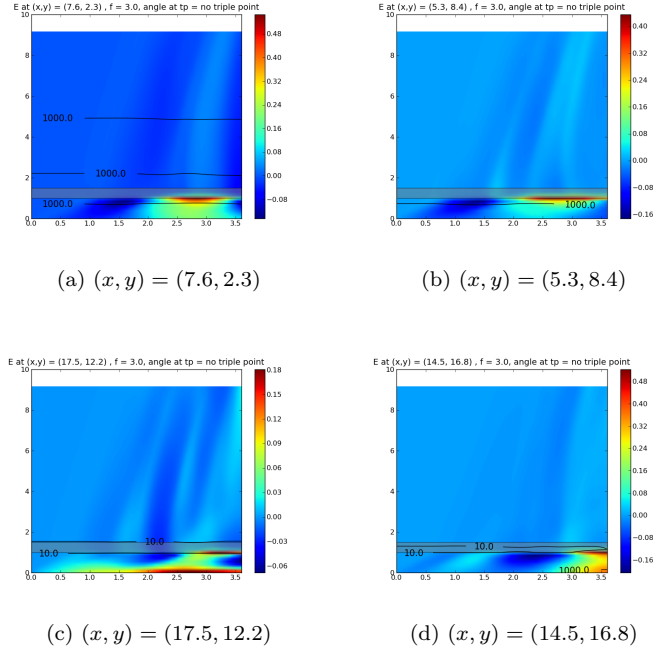


FIGURE 22. Relative change in total energy (as a function of height and time) at four different horizontal locations in the three dimensional experiment with observed magnetic field and driving. All the results are with a second-order accurate scheme on a mesh of $120 \times 120 \times 60$ points.

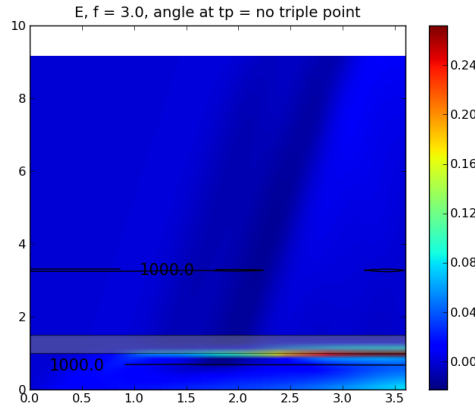


FIGURE 23. Relative change in total energy, integrated across all horizontal locations, vs. time in the 3-D observed case.

more of the pressure waves are stuck in the transition region than in the high frequency case.

In three space dimensions, we perform simulations with both synthetic and observed magnetic fields. An important difference from the two-dimensional case is the possibility of two transverse wave modes in three space dimensions. We follow Carlsson and Bogdan (2006) and plot the velocity in the principal normal and binormal directions to the magnetic field in order to detect both transverse wave types. The three-dimensional results are summarized below.

- Wave dynamics is strongly dependent on the nature of the forcing. For vertical forcing at the bottom boundary, we observe that waves along the magnetic field are present throughout the domain. On the other hand, transverse waves exist only when the field is strong compared to the gas pressure. Although there are substantial differences between waves in the two transverse directions, we were unable to obtain direct evidence for the presence of Alfvén waves in the case of vertical driving. There are pressure jumps across the transverse waves indicating that they are fast waves.
- When the bottom boundary is forced in the transverse direction, the wave dynamics are very different. In particular, we observe a clear separation between slow mode waves and transverse waves that travel at a faster speed. The slow mode waves spiral along the magnetic field. The transverse waves are directed upward along the magnetic field. There is no pressure jump across the transverse waves indicating the existence of coronal Alfvén waves in this configuration. This should be contrasted with the other papers describing numerical simulations like Carlsson and Bogdan (2006) which provide only indirect evidence for the possible presence of Alfvén waves.
- There is a rich spatial variation in the energy transferred by upward moving waves in three space dimensions. The energy transfer seems to depend on the magnetic field strength at a given horizontal location.
- The energy dynamics shows differences in detail between the vertical forcing and the transverse forcing scenarios. However, the overall picture is quite similar. Most of the incident energy is accumulated at the base of the transition region and in the chromosphere. This energy is carried by waves that move horizontally along the transition layer. Some of the wave energy is transmitted into the corona. The proportion of transmitted to incident energy is higher for the transverse forcing case.

We also consider a background magnetic field and a bottom forcing that were observed by SOHO and perform a simulation with this observed data set as input. The wave dynamics are much more complicated and there is evidence for the existence of all wave modes. However, the gross energy transfer landscape is very similar to the synthetic test cases. It shows that a large proportion of the wave energy is accumulated in the chromosphere providing a plausible explanation for observed chromospheric heating. A smaller proportion of wave energy is transmitted into the corona. There is a clear evidence for the existence of different wave modes in the corona.

Our simulations show that realistic synthetic magnetic fields and synthetic bottom driving display very complex wave dynamics and provide reasonable explanations for phenomena like chromospheric heating, coronal waves, mode conversion at the magnetic canopy, and reflection and refraction at the transition layer. Furthermore, three dimensional simulations provide evidence for the existence of coronal Alfvén waves. These results should be considered as a step towards better understanding of solar observations. More physics, particularly radiation, needs to be added in our code in order to provide a better approximation to observations.

REFERENCES

- Banerjee, D., Erdelyi, R., Oliver, R., & O’Shea, E. 2007, *Solar Phys.*, 246, 3
 Bogdan, T.J., *et al.* 2003, *ApJ*, 599, 626
 Cally, P. 2001, *ApJ*, 548, 473
 Cally, P. 2006, *Phil. Trans. R. Soc.*, 364
 Carlsson, M., & Bogdan, T.J. 2006, *Phil. Trans. R. Soc.*, 364, 395
 Carlsson, M., & Stein, R.F. 2002, in *Magnetic Couple of the Solar Atmosphere*, ed. H. Sawaya-Lacoste (ESA SP-505), 293
 De Pontieu, B., Erdelyi, R., & De Wijn, A.G. 2003a, *ApJ*, 595, 63
 De Pontieu, B., Tarbell, T., & Erdelyi, R. 2003b, *ApJ*, 590, 502
 Erdelyi, R., Malins, C., Toth, G., De Pontieu, B. 2007, *A&A*, 467, 1299
 Fedun, V., Erdelyi, R., Shelyag, S. 2009, *Solar Phys.*, 258, 219
 Finsterle, W., *et al.* 2004, *ApJ*, 613, 85
 Finsterle, W., Haberreiter, M., Kosovichev, S., & Schmutz, S. 2008, in *Proc. IAU Symp. 274, Waves and oscillations in the solar atmosphere: Heating and magneto-seismology*, ed R. Erdelyi *et al.*, 74
 Fuchs, F., McMurry, A.D., Mishra, S., Risebro, N.H., & Waagan, K. 2010a, *Comm. Comput. Phys.*, 7(3), 473
 Fuchs, F., McMurry, A.D., Mishra, S., Risebro, N.H., & Waagan, K. 2010b, *JCP*, 229 (11), 4033

- Fuchs, F., McMurry, A.D., Mishra, S., Risebro, N.H., & Waagan, K. 2011a, *Comm. Comput. Phys.*, in press (<http://www.sam.math.ethz.ch/reports/2009/37>)
- Fuchs, F., McMurry, A.D., Mishra, S., & Waagan, K. 2011b, <http://www.sam.math.ethz.ch/reports/2010/27>
- Gottlieb, S., Shu, C.W., & Tadmor, E. 2001, *SIAM Review*, 43, 89
- Gurski, K.F. 2004, *SIAM J. Sci. Comp.*, 25(6), 2165
- Hansteen, V., Carlsson, M., & Gudiksen, B. 2007, in CS-368, *The physics of chromospheric plasmas* (San Francisco), 107
- Hansteen, V., *et al.* 2006, *ApJ*, 647, 73
- Hasan, S., Ballegooijen, A., Kalkofen, W., & Steiner, O. 2007, *ApJ*, 666, 1277
- Hasan S., and Ballegooijen, A. 2008, *ApJ*, 680, 1542
- Khomenko, E., Collados, M., & Felipe, T. 2008, *Solar Phys.*, 251, 89
- LeVeque, R.J. 2002, *Finite volume methods for hyperbolic problems* (Cambridge, UK: Cambridge University Press)
- McIntosh, S.W., Fleck, B., & Judge, P.G. 2003, *A&A*, 405, 769
- McIntosh, S.W., Fleck, B., & Tarbell, T. 2004, *ApJ*, 609, 95
- McIntosh, S.W., *et al.* 2001, *ApJ*, 548, 237
- Nordlund, A., & Galsgaard, K. 1995, A 3D MHD code for parallel computers. (Tech. Rep. Astro. Obs. Univ. of Copenhagen)
- Rosenthal, C.S. *et al.* 2002, *ApJ*, 564, 508
- Roupe van der Voort, L., *et al.* 2005, *A&A*, 435, 327
- Toth, G. 2000, *JCP*, 161, 605
- Van Leer, B. 1979, *JCP*, 32, 101
- Vernazza, J., Avrett, E., & Loeser, R. 1981, *ApJS*, 45, 636
- Zhugzhda, I.D., & Dzhililov, N.S. 1984, *A&A*, 132, 45
- Zhugzhda, I.D., & Dzhililov, N.S. 1984, *A&A*, 132, 52

APPENDIX A: NUMERICAL SCHEMES

We approximate the system (2.3) in a Cartesian domain $\mathbf{x} = (x, y, z) \in [X_l, X_r] \times [Y_l, Y_r] \times [Z_b, Z_t]$ and discretize it by a uniform grid in all directions with the grid spacing $\Delta x, \Delta y$ and Δz . We set $x_i = X_l + i\Delta x$, $y_j = Y_l + j\Delta y$ and $z_k = Z_b + k\Delta z$. The indices are $0 \leq i \leq N_x$, $0 \leq j \leq N_y$ and $0 \leq k \leq N_z$. Set $x_{i+1/2} = x_i + \Delta x/2$, $y_{j+1/2} = y_j + \Delta y/2$ and $z_{k+1/2} = z_k + \Delta z/2$, hence a typical cell may be denoted $\mathcal{C}_{i,j,k} = [x_{i-1/2}, x_{i+1/2}] \times [y_{j-1/2}, y_{j+1/2}] \times [z_{k-1/2}, z_{k+1/2}]$. The cell average of the unknown state vector \mathbf{W} (approximating \mathbf{U}) over $\mathcal{C}_{i,j,k}$ at time t is denoted $\mathbf{W}_{i,j,k}(t)$. We will approximate (2.1) with second-order accurate finite volume scheme. Given the cell averages $\mathbf{W}_{i,j,k}(t)$, the semi-discrete form of the second order scheme is given by

$$(6.1) \quad \frac{d}{dt} \mathbf{W}_{i,j,k} = \mathcal{F}_{i,j,k} = -\frac{1}{\Delta x} (\tilde{\mathbf{F}}_{i+1/2,j,k} - \tilde{\mathbf{F}}_{i-1/2,j,k}) - \frac{1}{\Delta y} (\tilde{\mathbf{G}}_{i,j+1/2,k} - \tilde{\mathbf{G}}_{i,j-1/2,k}) \\ - \frac{1}{\Delta z} (\tilde{\mathbf{H}}_{i,j,k+1/2} - \tilde{\mathbf{H}}_{i,j,k-1/2}) + \tilde{\mathbf{S}}_{i,j,k}^1 + \tilde{\mathbf{S}}_{i,j,k}^2 + \tilde{\mathbf{S}}_{i,j,k}^3 + \mathbf{S}_{i,j,k}^g.$$

The numerical fluxes $\mathbf{F}, \mathbf{G}, \mathbf{H}$ and the sources $\tilde{\mathbf{S}}^{1,2,3}$ are defined below. The time dependence in the above expression is suppressed for notational convenience.

It is standard (LeVeque 2002) to replace the piecewise constant approximation $\mathbf{W}_{i,j,k}$ with a non-oscillatory piecewise linear reconstruction in-order to obtain second-order spatial accuracy. There are a variety of reconstructions including the popular TVD-MUSCL limiters (Van Leer 1979). However, we need (6.1) to preserve a suitable discrete version of the steady state (2.7) and a standard reconstruction of the conservative variables does not lead to such a well-balanced scheme.

Consequently we now modify the novel *equilibrium variables* based reconstruction algorithm of Fuchs *et al.* (2010b) to the setting of non-isothermal atmospheres. Given the cell averages $\mathbf{W}_{i,j,k}$ at any given time, we define a piecewise constant temperature distribution by (2.4) and denote the cell temperature as $T_{i,j,k}$. We have the following reconstruction algorithms.

6.1. Minmod reconstruction (MM). Given the cell values $q_{i,j,k}$ of a state variable q , denote the *minmod* derivative in the x -direction as

$$(6.2) \quad D^x q_{i,j,k} = \text{minmod} \left(\frac{q_{i+1,j,k} - q_{i,j,k}}{\Delta x}, \frac{q_{i,j,k} - q_{i-1,j,k}}{\Delta x} \right),$$

$$\text{minmod}(a, b) = \frac{1}{2} (\text{sgn}(a) + \text{sgn}(b)) \min(|a|, |b|).$$

The minmod derivatives $D^y q_{i,j,k}$ and $D^z q_{i,j,k}$ in the remaining directions are defined analogously. Then, a piecewise linear *non-oscillatory* approximation of q is of the form,

$$(6.3) \quad q = q_{i,j,k}(x, y, z) = q_{i,j,k} + D^x q(x - x_i) + D^y q(y - y_j) + D^z q(z - z_k), \quad (x, y, z) \in \mathcal{C}_{i,j,k}.$$

From the cell values of ρ , \mathbf{u} and \mathbf{B} , we define the minmod slopes by (6.2) and obtain the corresponding piecewise linear approximations of these variables by (6.3). However, a minmod reconstruction of the pressure does not lead to a well balanced scheme. We need a novel pressure reconstruction, based on a corresponding reconstruction of the temperature.

Given the cell averages $\mathbf{W}_{i,j,k}$, we compute the cell temperature $T_{i,j,k}$ by (2.4). We reconstruct the temperature as a piecewise linear function taking the values $T_{i,j,k}$ at the cell centers. This piecewise linear temperature can be used to compute the corresponding α function by (2.6). However, we only need the differences in α given by,

$$(6.4) \quad \alpha_{i,j,k+\lambda} - \alpha_{i,j,k} = \int_{z_k}^{z_{k+\lambda}} \frac{1}{\hat{T}_{i,j}(z)} dz = \frac{\Delta z}{T_{i,j,k+1} - T_{i,j,k}} \log \left(\frac{\hat{T}_{i,j}(z_{k+\lambda})}{T_{i,j,k}} \right), \quad \lambda \in \{1/2, 1\}.$$

Note that the difference in α is always well-defined and for $T_{i,j,k+1} = T_{i,j,k}$ degenerates to

$$(6.5) \quad \alpha_{i,j,k+\lambda} - \alpha_{i,j,k} = (z_{i,j,k+\lambda} - z_{i,j,k}) / T_{i,j,k}, \quad \lambda \in \{1/2, 1\}.$$

We use the α function to reconstruct the pressure.

As in Fuchs *et al.* (2010b), we define

$$(6.6) \quad \mathbf{L}p_{i,j,k} = \log(p_{i,j,k}),$$

and compute the minmod derivatives $D^{x,y} \mathbf{L}p$ by (6.2). A scaled minmod derivative in the z -direction takes the form,

$$(6.7) \quad D^z \mathbf{L}p_{i,j,k} = \text{minmod} \left(\frac{\mathbf{L}p_{i,j,k+1} - \mathbf{L}p_{i,j,k}}{\alpha_{i,j,k+1} - \alpha_{i,j,k}}, \frac{\mathbf{L}p_{i,j,k} - \mathbf{L}p_{i,j,k-1}}{\alpha_{i,j,k} - \alpha_{i,j,k-1}} \right),$$

where the difference in α is computed in (6.4). Then a piecewise linear approximation of the pressure is computed by

$$(6.8) \quad p(x, y, z) = p_{i,j,k} e^{D^x \mathbf{L}p_{i,j,k}(x-x_i)} e^{D^y \mathbf{L}p_{i,j,k}(y-y_j)} e^{D^z \mathbf{L}p_{i,j,k}(\alpha(z)-\alpha(z_k))},$$

where α is again computed from (6.4). The cell edge values of the conservative variables can be easily obtained from the piecewise linear approximations of the primitive variables. The minmod limiter is one possible choice among many reconstruction procedures. Other limiters like the MC, superbee, ENO and WENO limiters can be modified analogously

We denote the reconstructed piecewise linear conservative variables in the cell $\mathcal{C}_{i,j,k}$ as $\mathbf{W}_{i,j,k}(x, y, z)$, define the following cell edge values,

$$\begin{aligned} \mathbf{W}_{i,j,k}^E &= \mathbf{W}_{i,j,k}(x_{i+1/2}, y_j, z_k), & \mathbf{W}_{i,j,k}^W &= \mathbf{W}_{i,j,k}(x_{i-1/2}, y_j, z_k), \\ \mathbf{W}_{i,j,k}^N &= \mathbf{W}_{i,j,k}(x_i, y_{j+1/2}, z_k), & \mathbf{W}_{i,j,k}^S &= \mathbf{W}_{i,j,k}(x_i, y_{j-1/2}, z_k), \\ \mathbf{W}_{i,j,k}^t &= \mathbf{W}_{i,j,k}(x_i, y_j, z_{k+1/2}), & \mathbf{W}_{i,j,k}^b &= \mathbf{W}_{i,j,k}(x_i, y_j, z_{k-1/2}), \end{aligned}$$

and define the numerical fluxes by

$$(6.9) \quad \begin{aligned} \tilde{\mathbf{F}}_{i+1/2,j,k} &= \mathbf{F} \left(\mathbf{W}_{i,j,k}^E, \mathbf{W}_{i+1,j,k}^W, \tilde{\mathbf{B}}_{i+1/2,j,k} \right), & \tilde{\mathbf{G}}_{i,j+1/2,k} &= \mathbf{G} \left(\mathbf{W}_{i,j,k}^N, \mathbf{W}_{i,j+1,k}^S, \tilde{\mathbf{B}}_{i,j+1/2,k} \right), \\ \tilde{\mathbf{H}}_{i,j,k+1/2} &= \mathbf{H} \left(\mathbf{W}_{i,j,k}^t, \mathbf{W}_{i,j,k+1}^b, \tilde{\mathbf{B}}_{i,j,k+1/2} \right), \end{aligned}$$

The value of the staggered coefficient $\tilde{\mathbf{B}}$ is given by a simple evaluation,

$$\tilde{\mathbf{B}}_{i+1/2,j,k} = \tilde{\mathbf{B}}(x_{i+1/2}, y_j, z_k), \quad \tilde{\mathbf{B}}_{i,j+1/2,k} = \tilde{\mathbf{B}}(x_i, y_{j+1/2}, z_k), \quad \tilde{\mathbf{B}}_{i,j,k+1/2} = \tilde{\mathbf{B}}(x_i, y_j, z_{k+1/2}),$$

This choice ensures formal second order accuracy for a smooth background magnetic field.

6.2. Numerical fluxes. Following Fuchs *et al.* (2010b, 2011a), we determine the numerical flux $\mathbf{F}_{i+1/2,j,k}$ and the source term $\mathbf{S}_{i,j,k}^1$ (in the x -direction) from the (approximate) solution of the following Riemann problem

$$(6.10) \quad \mathbf{W}_t + \mathbf{f}(\mathbf{W}, \tilde{\mathbf{B}}_M)_x = \mathbf{s}^1(\mathbf{W}, \tilde{\mathbf{B}}_M, \mathbf{W}_x), \quad \mathbf{W}(x, 0) = \begin{cases} \mathbf{W}_L & x < 0, \\ \mathbf{W}_R & x > 0, \end{cases}$$

We will approximate the eight waves in the MHD Riemann problem with three waves, i.e, two representing the outermost fast waves and a middle wave approximating the material contact discontinuity. The approximate solution and fluxes are given by

$$(6.11) \quad \mathbf{W}^{H_3} = \begin{cases} \mathbf{W}_L & \text{if } \frac{x}{t} \leq s_L, \\ \mathbf{W}_L^* & \text{if } s_L < \frac{x}{t} < s_M, \\ \mathbf{W}_R^* & \text{if } s_M < \frac{x}{t} < s_R, \\ \mathbf{W}_R & \text{if } s_R \leq \frac{x}{t}, \end{cases} \quad \mathbf{F}^{H_3} = \begin{cases} \mathbf{F}_L & \text{if } \frac{x}{t} \leq s_L, \\ \mathbf{F}_L^* & \text{if } s_L < \frac{x}{t} < s_M, \\ \mathbf{F}_R^* & \text{if } s_M < \frac{x}{t} < s_R, \\ \mathbf{F}_R & \text{if } s_R \leq \frac{x}{t}. \end{cases}$$

We set $\pi_1 = p + \frac{\bar{B}_2^2 + \bar{B}_3^2}{2}$. The outer wave speeds s_L and s_R model the fast magneto-sonic waves and are defined as in Gurski (2004). In order to describe the solver, we need to determine the speed of the middle wave s_M and the intermediate states $\mathbf{W}_L^*, \mathbf{W}_R^*$. The middle wave models a material contact discontinuity. Hence, the velocity field and the tangential magnetic fields are assumed to be constant across the middle wave. This allows us to define $\mathbf{u}^* = \mathbf{u}_L^* = \mathbf{u}_R^*$, $\bar{B}_2^* = \bar{B}_{2L}^* = \bar{B}_{2R}^*$ and $\bar{B}_3^* = \bar{B}_{3L}^* = \bar{B}_{3R}^*$. The normal magnetic field \bar{B}_1 is not assumed to be constant but jumps only across the middle wave (modeling the linear degenerate ‘‘divergence wave’’ and \bar{B}_1 is constant across the outer waves. The intermediate states are determined by local conservation across the two outermost waves and the middle wave resulting in,

$$(6.12) \quad s_\sigma \mathbf{W}_\sigma^* - \mathbf{F}_\sigma^* = s_\sigma \mathbf{W}_\sigma - \mathbf{F}_\sigma, \quad s_M \mathbf{W}_R^* - s_M \mathbf{W}_L^* = \mathbf{F}_R^* - \mathbf{F}_L^* + \mathbf{s}^{1,*}$$

where $\sigma \in \{L, R\}$ and

$$(6.13) \quad \mathbf{s}^{1,*} = \begin{pmatrix} 0 \\ -\frac{\bar{B}_{1R}^2 - \bar{B}_{1L}^2}{2} \\ -\left(\bar{B}_2^*\right) (\bar{B}_{1R} - \bar{B}_{1L}) \\ -\left(\bar{B}_3^*\right) (\bar{B}_{1R} - \bar{B}_{1L}) \\ -\mathbf{u}^* (\bar{B}_{1R} - \bar{B}_{1L}) \\ -u_1^* \frac{\bar{B}_{1R}^2 - \bar{B}_{1L}^2}{2} - \left(u_2^* \bar{B}_2^* + u_3^* \bar{B}_3^*\right) (\bar{B}_{1R} - \bar{B}_{1L}) \end{pmatrix}.$$

This amounts to integrating the source \mathbf{s}^1 across the wave fan.

Applying the conservation relations, we obtain (check Fuchs *et al.* (2010b), section 3.1.2 for details) the following intermediate states,

$$\begin{aligned}
\rho_\theta^* &= \rho_\theta \frac{u_{1\theta} - s_\theta}{s_M - s_\theta}, \quad \pi_{1\theta}^* = \pi_{1\theta} + \rho_\theta(u_{1\theta} - s_\theta)(u_{1\theta} - s_M), \quad \theta \in \{L, R\}, \\
s_M = u_1^* &= \frac{\pi_{1R} - \pi_{1L} + \rho_R u_{1R}(u_{1R} - s_R) - \rho_L u_{1L}(u_{1L} - s_L)}{\rho_R(u_{1R} - s_R) - \rho_L(u_{1L} - s_L)}, \\
u_\sigma^* &= \frac{\zeta c_\sigma - \xi d_\sigma}{\alpha \zeta + \xi^2}, \quad \bar{B}_\sigma^* = \frac{-\alpha d_\sigma - \xi c_\sigma}{\alpha \zeta + \xi^2}, \quad \sigma \in \{2, 3\} \\
E_\theta^* &= \frac{1}{s_M - s_\theta} \left(E_\theta(u_{1\theta} - s_\theta) + \pi_{1\theta} u_{1\theta} - \pi_{1\theta}^* s_M + \frac{\bar{B}_{1\theta}^2}{2} (u_{1\theta} - s_M) \right. \\
&\quad \left. + (\bar{B}_{1\theta}) \left(\bar{B}_{2\theta} u_{2\theta} + \bar{B}_{3\theta} u_{3\theta} - \bar{B}_{2\theta}^* u_{2\theta}^* - \bar{B}_{3\theta}^* u_{3\theta}^* \right) \right), \quad \theta \in \{L, R\}, \\
c_\sigma &= \rho_R u_{\sigma R}(u_{1R} - s_R) - \rho_L u_{\sigma L}(u_{1L} - s_L) - (\bar{B}_{1R} \bar{B}_{\sigma R} - \bar{B}_{1L} \bar{B}_{\sigma L}), \\
d_\sigma &= \bar{B}_{\sigma R}(u_{1R} - s_R) - \bar{B}_{\sigma L}(u_{1L} - s_L) - (\bar{B}_{1L} u_{\sigma L} - \bar{B}_{1R} u_{\sigma R}), \\
\alpha &= \rho_R(u_{1R} - s_R) - \rho_L(u_{1L} - s_L), \quad \zeta = s_R - s_L, \quad \xi = \bar{B}_{1R} - \bar{B}_{1L}.
\end{aligned}$$

The intermediate fluxes are obtained in terms of the intermediate states by local conservation (6.12),

$$\mathbf{F}_L^* = \mathbf{F}_L + s_L(\mathbf{W}_L^* - \mathbf{W}_L), \quad \mathbf{F}_R^* = \mathbf{F}_R + s_R(\mathbf{W}_R^* - \mathbf{W}_R).$$

The discrete source term takes the form,

$$(6.14) \quad \mathbf{S}_i^{1,n} = \mathbf{s}_{i-1/2}^{1,*} \chi_{(s_M, i-1/2 \geq 0)} + \mathbf{s}_{i+1/2}^{1,*} \chi_{(s_M, i+1/2 < 0)},$$

where $\mathbf{s}_{i\pm 1/2}^{1,*}$ is defined in analogy to (6.13).

For the three dimensional form of the equations, the fluxes \mathbf{G}, \mathbf{H} and the sources \mathbf{S}^2 and \mathbf{S}^3 can be defined analogously. The discretized gravity source term \mathbf{S}^g is given by,

$$(6.15) \quad \mathbf{S}_{i,j,k}^g = \left\{ 0, 0, \frac{p_{i,j,k}^t - p_{i,j,k}^b}{\Delta z}, 0, 0, 0, 0, -\rho_{i,j,k}^n (u_3^n)_{i,j,k} g \right\}.$$

6.2.1. Boundary conditions for the second order scheme. The boundary is treated in the following way. We need to specify two layers of ghost cells in each direction for a second order scheme. We use periodic boundary conditions in the x - and y - directions, i.e., for $1 \leq j \leq N_y$ and $1 \leq k \leq N_z$, we have

$$(6.16) \quad \mathbf{W}_{0,j,k} = \mathbf{W}_{N_x,j,k}, \quad \mathbf{W}_{-1,j,k} = \mathbf{W}_{N_x-1,j,k}, \quad \mathbf{W}_{N_x+1,j,k} = \mathbf{W}_{1,j,k}, \quad \mathbf{W}_{N_x+2,j,k} = \mathbf{W}_{2,j,k}$$

The ghost cell values in the y -direction can be defined analogously.

In the z -direction, we use second-order extrapolated Neumann boundary conditions for the velocity and the magnetic field, i.e., for $\mathbf{w} = \{\mathbf{u}, \mathbf{B}\}$,

$$(6.17) \quad \mathbf{w}_{i,j,d} = \mathbf{w}_{i,j,1}, \quad \mathbf{w}_{i,j,N_z+2+d} = \mathbf{w}_{i,j,N_z}$$

for $1 \leq i \leq N_x$, $1 \leq j \leq N_y$ and $d \in \{0, -1\}$ in order to define the values in the ghost cells.

The pressure and the density in the ghost cells are extrapolated in terms of its logarithm $\mathbf{L}p = \log(p)$ and $\mathbf{L}\rho = \log(\rho)$ according to (6.8) and simplify to

$$(6.18) \quad \begin{aligned} p_{i,j,d} &= p_{i,j,1} e^{(\alpha_{i,j,d} - \alpha_{i,j,1})/H}, & p_{i,j,N_z+2+d} &= p_{i,j,N_z} e^{(\alpha_{i,j,N_z+2+d} - \alpha_{i,j,N_z})/H}, \\ \rho_{i,j,d} &= \rho_{i,j,1} e^{(\alpha_{i,j,d} - \alpha_{i,j,1})/H}, & \rho_{i,j,N_z+2+d} &= \rho_{i,j,N_z} e^{(\alpha_{i,j,N_z+2+d} - \alpha_{i,j,N_z})/H}, \end{aligned}$$

where the differences in α are given by (6.5). This amounts to using a scaled version of the extrapolated Neumann type boundary conditions of Fuchs *et al.* (2010a) for the primitive variables.

6.2.2. *Time Stepping.* The standard scheme for a first order approximation in time is the forward Euler time stepping, formally written as

$$\mathbf{W}_{i,j,k}^{n+1} = \mathbf{W}_{i,j,k}^n + \Delta t^n \mathcal{F}_{i,j,k}^n$$

where $\mathcal{F}_{i,j,k}^n$ is defined in (6.1). For second-order schemes, we use the second-order strong-stability preserving Runge-Kutta (SSP) time stepping (Gottlieb *et al.* 2001)

$$\begin{aligned} \mathbf{W}_{i,j,k}^* &= \mathbf{W}_{i,j,k}^n + \Delta t^n \mathcal{F}_{i,j,k}^n, \\ \mathbf{W}_{i,j,k}^{**} &= \mathbf{W}_{i,j,k}^* + \Delta t^n \mathcal{F}_{i,j,k}^*, \\ \mathbf{W}_{i,j,k}^{n+1} &= \frac{1}{2}(\mathbf{W}_{i,j,k}^n + \mathbf{W}_{i,j,k}^{**}). \end{aligned}$$

The time step is determined by a standard CFL condition.

The scheme (6.1) as constructed above is shown to be second-order accurate and is well balanced i.e, it preserves a discrete version of the steady state (2.7). The proof of these properties is presented in Fuchs *et al.* (2011b).

(Franz Georg Fuchs) CENTRE OF MATHEMATICS FOR APPLICATIONS (CMA)
UNIVERSITY OF OSLO
P.O. BOX 1053, BLINDERN
N-0316 OSLO, NORWAY
E-mail address: franzgeorgfuchs@gmail.com
URL: <http://folk.uio.no/franzf/>

(Andrew D. McMurry) CENTRE OF MATHEMATICS FOR APPLICATIONS (CMA)
UNIVERSITY OF OSLO
P.O. BOX 1053, BLINDERN
N-0316 OSLO, NORWAY
E-mail address: a.d.mcmurry@ifi.uio.no

(Siddhartha Mishra) SEMINAR FOR APPLIED MATHEMATICS (SAM)
ETH ZÜRICH,
RÄMISTRASSE 101,
ZÜRICH-8044, SWITZERLAND
E-mail address: siddharm@cma.uio.no

(Knut Waagan) CENTER FOR SCIENTIFIC COMPUTATION AND MATHEMATICAL MODELING (CSCAMM)
UNIVERSITY OF MARYLAND,
CSIC BUILDING 406,
COLLEGE PARK MD:20742-3289, U.S.A
E-mail address: kwaagan@cscamm.umd.edu